Helsinki University of Technology
Low Temperature Laboratory
Espoo 2005

Experiments on vortex dynamics in superfluid ^{3}He

Antti Finne

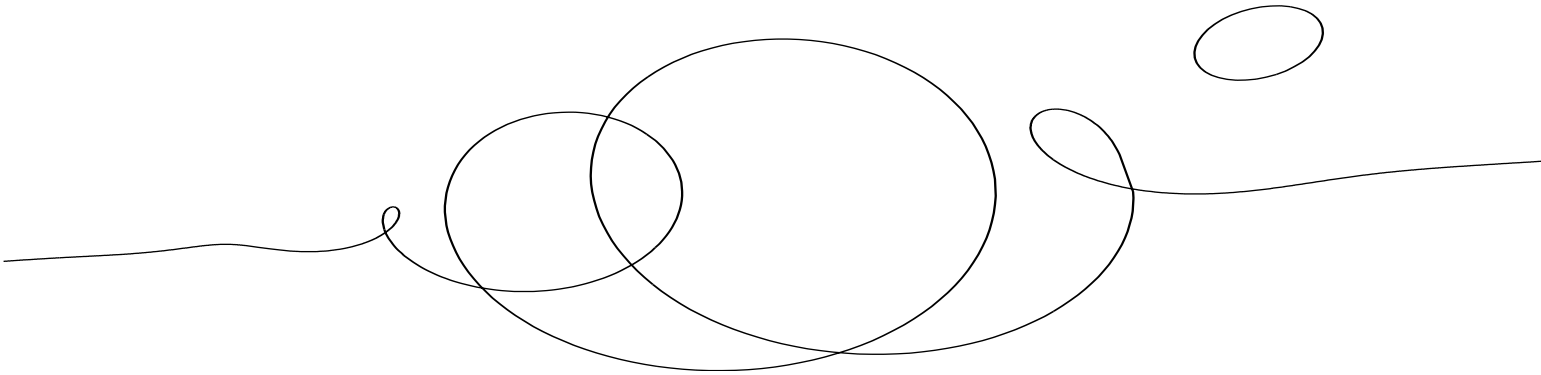

TEKNILLINEN KORKEAKOULU
TEKNISKA HÖGSKOLAN
HELSINKI UNIVERSITY OF TECHNOLOGY
TECHNISCHE UNIVERSITÄT HELSINKI
UNIVERSITE DE TECHNOLOGIE D'HELSINKI

Experiments on vortex dynamics in superfluid ^{3}He

Antti Finne

Dissertation for the degree of Doctor of Science in Technology to be presented with due permission of the Department of Engineering Physics and Mathematics for public examination and debate in Auditorium F1 at Helsinki University of Technology (Espoo, Finland) on the 23$^{\text{rd}}$ of September, 2005, at 12 o'clock noon.

Helsinki University of Technology
Department of Engineering Physics and Mathematics
Low Temperature Laboratory

Teknillinen korkeakoulu
Teknillisen fysiikan ja matematiikan osasto
Kylmälaboratorio

Distribution:
Helsinki University of Technology
Low Temperature Laboratory
P.O. Box 2200
FIN-02015 HUT
Tel. +358-9-451-2973
Fax. +358-9-451-2969
E-mail: Antti.Finne@hut.fi
This dissertation can be read at http://lib.hut.fi/Diss/

ISBN 951-22-7830-8
ISBN 951-22-7831-6(pdf)

HELSINKI UNIVERSITY OF TECHNOLOGY P.O. BOX 1000, FIN-02015 HUT http://www.hut.fi	ABSTRACT OF DOCTORAL DISSERTATION

Author Antti Pekka Finne

Name of the dissertation

EXPERIMENTS ON VORTEX DYNAMICS IN SUPERFLUID 3HE

Date of manuscript 17.5.2005	Date of the dissertation 23.09.2005
☐ Monograph	☑ Article dissertation (summary + original articles)

Department	Department of Engineering Physics and Mathematics
Laboratory	Low Temperature Laboratory
Field of research	Experimental condensed matter physics
Opponent(s)	Prof. W.F. Vinen
Supervisor	Prof. Pekka Hautojärvi
(Instructor)	Prof. Matti Krusius

Abstract

There are two stable isotopes of helium: helium-3 and helium-4. Both exhibit superfluidity at low temperatures, helium-3 at around 1 mK. The superfluidity brings some special features to the fluid, such as the possibility of frictionless mass flow and quantization of flow through vortex lines. This thesis consists of experiments performed on superfluid helium-3 under rotation, and on the vortex lines the rotation induces. The cylindrical sample is probed using nuclear magnetic resonance (NMR) and there is a possibility to stabilize two superfluid phases, the A phase and the B phase, simultaneously in the sample. We study two aspects: the dynamics of the phase boundary between the A and the B phases, and turbulent vortex dynamics in the B phase.

When a sample which consists of both the A and the B phases is rotated, a velocity difference in the superfluid components can form across the phase boundary. At a sufficiently high velocity the boundary becomes unstable towards wave formation, analogously to the Kelvin-Helmholtz instability in classical hydrodynamics (e.g. waves form on water while wind blows over the surface). In regular fluids their viscosity affects the instability, these experiments are the first demonstration of the instability in superfluids. We present measurements on the criterion for the instability, and how vortex lines cross the phase boundary as a result. The instability turned out to provide unprecedented flexibility in vortex injection into the B phase and is used in the study of turbulent vortex dynamics.

Many questions remain unanswered regarding classical turbulence. In a superfluid, turbulence is seen as a chaotic motion of vortex lines. Turbulence has been studied intensively in superfluid helium-4, the measurements in this thesis are one of the first to show turbulent flow in the B phase of helium-3. Experiments in helium-3 give new insight into turbulent vortex dynamics since the two fluids differ in their hydrodynamic properties, for example, in terms of damping of vortex motion, vortex formation, and the dynamics of the normal fluid background. We study which effects are important in the formation of a turbulent vortex network, how the vortex lines spread into the vortex free region, and finally how they relax into the equilibrium state. We identify a similarity parameter for the flow in an analogous fashion to the Reynolds number in normal fluid dynamics. Unlike in regular fluids, the hydrodynamic transition between regular and turbulent vortex dynamics appears to be controlled by intrinsic parameters only.

Keywords superfluid, helium-3, vortex dynamics, turbulence, Kelvin-Helmholtz instability

UDC	Number of pages 45
ISBN (printed) 951-22-7830-8	ISBN (pdf) 951-22-7831-6
ISBN (others)	ISSN

Publisher Picaset Oy

Print distribution

☑ The dissertation can be read at http://lib.hut.fi/Diss/ 2005/isbn9512278316

Acknowledgments

This thesis work was carried out in the Low Temperature Laboratory of the Helsinki University of Technology. I want to express my gratitude to the director of the laboratory, Prof. Mikko Paalanen, for giving me the opportunity for this thesis work. I am especially grateful to Prof. Matti Krusius who is the head of the ROTA group and my thesis instructor for all his patient advice. The other senior members of the group Vladimir Eltsov and Sergei Boldarev have also taught me a great deal. I owe much to the previous generation of graduate students in the ROTA group, R. Blaauwgeers, J.J. Ruohio, and R. Schanen. I am deeply grateful for all the advice the late Prof. M.M. Salomaa provided during my studies.

The theoretical work by N.B. Kopnin, J. Kopu, E. Thuneberg, and G.E. Volovik has been invaluable. I am grateful to Prof. M. Tsubota and his group in Osaka: T. Araki, R. Hänninen, and A. Mitani, who have provided the numerical work clarifying the vortex dynamics which were investigated in these measurements. Our visitors: L. Skrbek, G. Eska, Z. Janu, D. Kivotides, R. Haley, and A. Gordeev have all given their valuable contributions to this work. I am grateful to L. Grönberg and I. Suni at VTT for providing us with their expertise in thin film processing. I want to thank the pre-examiners of this thesis, V.V. Dmitriev and W. Schoepe, for their advice.

I have been fortunate to work with great fellow students, J. Viljas, L. Roscier, R. Lindell, K. Juntunen, M. Sillanpää, H. Junes, E. Pentti, A. Salmela, T. Ruokola, R. Tarkiainen, J. Kivioja, J. Martikainen, M. Kujala, and A. Kulvik. I have also benefitted from the advice and help from other senior scientists in the lab: H. Alles, P. Hakonen, A. Sebedash, I. Todoshchenko, and J. Tuoriniemi.

I want to thank the administrative and the technical staff for all their efforts: Pirjo Muukkonen, Liisi Pasanen, Teija Halme, Satu Pakarinen, Marja Holmström, Tuire Koivisto, and Peter Berglund. The people at the workshop Markku Korhonen, Seppo Kaivola, Juhani Kaasinen, and Hannu Kaukelin have skillfully crafted all the parts we have requested and the liquifier, Arvi Isomäki and Antti Huvila, have provided the endless amount of liquid helium these experiments have required.

I am grateful for the financial support from Vilho, Yrjö ja Kalle Väisälä foundation and Jenny ja Antti Wihurin foundation.

Finally I would like to express my gratitude to my parents, Pekka and Helena, for all the support and encouragement and to Suvi for all the love, support, and patience.

Otaniemi, May 2005

Antti Finne

List of publications

This thesis is based on the following original publications.

[P1] A. Finne, L. Grönberg, R. Blaauwgers, V.B. Eltsov, G. Eska, M. Krusius, J.J. Ruohio, R. Schanen, and I. Suni, *Superconducting Nb-film LC resonator*, Rev. Sci. Instrum. **72** (9), 3682 (2001). Copyright ©2001 American Institute of Physics.

We explore the possibility to use thin film fabrication techniques to construct a LC resonator for NMR measurements in superfluid ^{3}He. A set of superconducting resonators and coils is tested for their properties and suitability for NMR measurements.

[P2] R. Blaauwgeers, V.B. Eltsov, G. Eska, A.P. Finne, R.P. Haley, M. Krusius, J.J. Ruohio, L. Skrbek, G.E. Volovik, *Shear Flow and Kelvin-Helmholz instability in superfluid*, Phys. Rev. Lett. **89**, 155301 (2002). Copyright ©2002 American Physical Society.

Experimental results on the AB interface under rotation are discussed. They are explained in terms of an instability which is the analog of the Kelvin-Helmholtz instability in conventional hydrodynamics.

[P3] M. Krusius, A.P. Finne, R. Blaauwgeers, V.B. Eltsov, G.E. Volovik, *Vortex line connections across the AB interface in superfluid ^{3}He*, Physica B **329-333**, 91 (2003). Copyright ©2002 Elsevier Science.

The A phase of superfluid ^{3}He supports a number of vortex structures. In typical rotation experiments the dominant vortex structure is the double quantum vortex. Here we study how the singly quantized vortex is affected by the phase boundary.

[P4] V.B. Eltsov, R. Blaauwgeers, A.P. Finne, M. Krusius, J.J. Ruohio, G.E. Volovik, *Instabilitity of AB interfaces of different shapes in rotating ^{3}He*, Physica B **329-333**, 96 (2003). Copyright ©2003 Elsevier Science.

In this experiment it is possible to stabilize both the A and the B phase simultaneously in the sample using magnetic fields. The shape of the AB phase boundary is calculated and the appearance of a hole in the boundary is identified from the measurements.

[P5] R. Blaauwgeers, S. Boldarev, V.B. Eltsov, A.P. Finne, and M. Krusius, *Superfluid He in Rotation: Single-Vortex Resolution and Requirements on Rotation*, J. Low Temp. Phys **132**, 263 (2003). Copyright ©2003 Springer Science and Business Media.

We study the quality of rotation in the ROTA cryostat and discuss how instabilities in the rotation velocity from mechanical resonances affect the NMR measurements.

[P6] R. Hänninen, R. Blaauwgeers, V.B. Eltsov, V.B. Eltsov, A.P. Finne, M. Krusius, E.V. Thuneberg, and G.E. Volovik, *Structure of the Surface Vortex Sheet between Two Rotating ^{3}He Superfluids*, Phys. Rev. Lett. **90**, 225301 (2003). Copyright ©2003 American Physical Society.

We calculate the bending of vortex lines or sheets on to the AB phase boundary and calculate numerically how the vorticity distributes itself as a surface sheet on the AB interface. This is compared to experimental results which indicate that vorticity penetrates through the AB phase boundary in single quantum units.

[P7] A.P. Finne, T. Araki, R. Blaauwgeers, V.B. Eltsov, N.B. Kopnin, M. Krusius, L. Skrbek, M. Tsubota, and G.E. Volovik, *An intrinsic velocity-independent criterion for superfluid turbulence*, Nature **424**, 1022 (2003).

Measurements on the nature of vortex dynamics are discussed as a function of mutual friction damping in rotating superfluid ^{3}He-B at 29 bar pressure. An intrinsic parameter of the liquid is identified which controls the transition from regular to turbulent vortex dynamics similar to the Reynolds number in classical hydrodynamics.

[P8] A.P. Finne, V.B. Eltsov, R. Blaauwgeers, Z. Janu, M. Krusius, L. Skrbek, *Time-of-Flight Measurements on Quantized Vortex Lines in Rotating ^{3}He-B*, J. Low Temp. Phys. **134**, 375 (2004). Copyright ©2004 Springer Science and Business Media.

We measure the time of flight of vortex lines when they expand into rotating vortex free counterflow. Regardless of the number of vortex lines in the front which travels in the rotating column, we find the longitudinal velocity to be $v_{L,z} = \alpha\Omega R$, where α is the damping in vortex motion, Ω the rotation velocity, and R the radius of the sample.

[P9] A.P. Finne, S. Boldarev, V.B. Eltsov, M. Krusius, *Vortex formation in neutron-irradiated rotating superfluid ^{3}He-B*, J. Low Temp. Phys. **135**, 479 (2004). Copyright ©2004 Springer Science and Business Media.

We describe measurements where neutron irradiation is used for vortex injection. The measurements demonstrate that the initial vortex configuration at injection is important in the onset of turbulence.

[P10] A.P. Finne, S. Boldarev, V.B. Eltsov, M. Krusius, *Measurement of turbulence in superfluid ^{3}He-B*, J. Low Temp. Phys. **136**, 249 (2004). Copyright ©2004 Springer Science and Business Media.

Techniques and results in measurements of turbulence are discussed. The KH instability is used as vortex injection mechanism.

[P11] A.P. Finne, S. Boldarev, V.B. Eltsov, M. Krusius, *Phase diagram of turbulence in superfluid ^{3}He-B*, J. Low Temp. Phys. **138**, 567 (2005). Copyright ©2005 Springer Science and Business Media.

This paper summarizes measurements on the transition in superfluid hydrodynamics from turbulent to regular (or vortex number conserving) dynamic processes as a function of increasing vortex damping at different pressures.

[P12] A.P. Finne, V.B. Eltsov, G. Eska, R. Hänninen, J. Kopu, M. Krusius, E.V. Thuneberg, and M. Tsubota, *Vortex Multiplication in Applied Flow: the Precursor to Superfluid Turbulence*, TKK-KYL-014 (2005).

We identify a vortex multiplication mechanism active at low damping and low vortex densities. The process is observed as a slow increase in vortex number which increases the vortex density to such level where superfluid turbulence in the bulk switches on.

[P13] A.P. Finne, V.B. Eltsov, R. Hänninen, J. Kopu, N. B. Kopnin, M. Krusius, E. V. Thuneberg, M. Tsubota, and G.E. Volovik *Vortex formation and dynamics in rotating superfluid ^{3}He-B below 0.6 T_c*, TKK-KYL-015 (2005).

This paper reviews our measurements where the evolution of seed vortex loops is investigated after they have been introduced in a long column of rotating vortex free ^{3}He-B.

Author's contribution

The work described in this thesis is experimental and was performed during the years 1999-2005 in the ROTA group of the Low Temperature Laboratory. For most of this time the experimental group consisted of 3-4 researchers. Also a number of researchers doing theoretical work as well as short term visitors have contributed to this work. The measurements in [P1] were done by me while I was working on my masters thesis. I started as graduate student in late 2000 but was absent the first half of 2001. Since autumn 2001 I was the only graduate student working full time on the experiment and responsible for the operation of the cryostat.

I took part in all the experiments and initial data analysis. The data analysis in the reports concerning turbulence ([P7], [P8], [P10], [P11], and [P13]) is to a large part done by me. The beginning of [P9] (chap. 1&2) is based on work and measurements prior to my involvement.

In 2004 I spent a considerable amount of time in the renovation work of the ROTA cryostat. The measurements and data analysis on the quality of rotation [P5] were done to a large part by me. I took part in the writing process of the papers to varying extent, but by discussing and commenting I was involved in the preparation of all manuscripts. I wrote an early version of [P7] as a conference proceedings paper which was subsequently withdrawn and reworked. [P1] and [P13] were written by me.

Contents

1 Introduction

Helium is the second most common element in the universe after hydrogen. It exists as two stable isotopes: ^{3}He and ^{4}He. After the Big Bang nuclear synthesis, roughly one quarter of the baryonic matter ended up as ^{4}He while only a fraction $\sim 10^{-5}$ of the mass became ^{3}He. On earth ^{4}He is found for example in natural gas wells where it has originated from radioactive decay. Again ^{3}He is the less common of the two isotopes: Only a few ppm of ^{3}He are present in the natural helium on earth. The ^{3}He used in laboratory experiments is a decay product of tritium which is used for example in fusion experiments and hydrogen bombs. For physics research it became available in the early sixties.

The helium liquids have the lowest boiling points of the natural elements. ^{4}He liquifies at 4.2 K and ^{3}He at 3.2 K at atmospheric pressure. They are special since even on cooling to absolute zero they do not solidify under ambient pressure. Only by applying high pressures can they be solidified. A special quantum effect, superfluidity, emerges in these liquids at low temperatures.

Heike Kamerlingh-Onnes managed to liquify ^{4}He in 1908 and later, by pumping the vapor, he cooled the liquid bath well below the superfluid transition, the λ-point at 2.17 K. However, it was only in 1939 (Ref. [1]) when it was realized that ^{4}He became a superfluid below the λ-transition. The ^{4}He atom is a boson and superfluidity arises when a macroscopic fraction of atoms occupies the minimum energy state in a process related to Bose-Einstein condensation. The superfluid state of ^{4}He is usually referred to as He-II. Superfluidity and superconductivity are related phenomena although the mechanism how the particles form a condensate depends on whether they are bosons or fermions. Whereas in a superconductor the electrons transport current without resistance, in a superfluid entire atoms condense to the superfluid state and move without resistance. The superfluid condensate flows without viscosity.

^{3}He is a composite fermion with spin 1/2 and the mechanism behind superfluidity is essentially different from ^{4}He. ^{3}He becomes superfluid through Cooper pairing similarly to electrons in a superconductor. In ^{3}He the superfluid transition is at much lower temperature than in ^{4}He, at maximum around 2.5 mK close to the solidification pressure of 34 bar. Partly for this reason, the superfluid transition, which was expected, remained undetected until 1972 [2].

Superfluid ^{3}He provides a unique test bed for the study of quantum effects. There are several phases and the order parameter allows numerous different types of topological defects. It is an extremely pure system, since the ^{3}He superfluid expels all impurities. Most importantly, there is an excellent theoretical understanding of its properties. In addition to being a fascinating system on its own, it can been employed as an analog model for

testing theories in other fields of physics [3]. A well-known example is an analog experiment on cosmic string formation in the phase transitions of the rapidly expanding Early Universe after the Big Bang [4].

This thesis studies the remarkable properties of superfluid ^{3}He and its topological defects. We address two different aspects in these measurements which are all performed with the same experimental setup: First, the shear-flow instability of the phase boundary between two superfluid phases ^{3}He-A and ^{3}He-B. This so-called AB interface is studied under rotation. Secondly, vortex dynamics in the B-phase of ^{3}He at low temperatures. In this latter work the shear flow instability provides a means to inject vortex loops into vortex free flow. After the injection the evolution and propagation of the vorticity is measured.

The AB boundary becomes unstable towards wave formation in differential shear flow of the two superfluid phases. In classical hydrodynamics this is known as the Kelvin-Helmholtz instability and it has numerous examples in nature, like wave formation on the surface of a lake on a windy day. However, in the classical case the instability is always affected by the viscosity of the fluids and the comparison to the ideal case is not straight forward. In our experiment we use the A and the B phases to create a "superfluid wind" at the phase boundary and observe when the boundary becomes unstable. This experiment is the first realization of such an instability with superfluids where there is no viscosity.

The second part of this thesis deals with one of the final unsolved fields in classical physics: turbulence. We study turbulent flow in a special subset of fluids, the superfluids. The superfluid condensate has no viscosity and the flow is quantized into topologically stable vortex lines. Because of these special features superfluid turbulence is sometimes called quantum turbulence. Superfluid turbulence has been studied for decades in He-II. We study the B phase of superfluid ^{3}He, where prior to us, only one experiment on the flow created with an oscillating wire has detected turbulence. We hope that the differences in the properties of He-II, ^{3}He-B, and classical viscous liquids, shed new light on the complex phenomenon of turbulent flow.

This preface of the thesis contains an introduction to the experiments and also some additional information not published in the research articles. The Introduction, Sec. 1, explains some of the relevant properties and concepts of superfluid ^{3}He. Section 2 introduces the experimental setup. In Sec. 3 some aspects of the shear flow instability are discussed and it also serves as an introduction to Sec. 4 which deals with experiments on turbulent vortex dynamics. Papers [P1] and [P5] focus on the technical development of the experiment. The shear-flow instability is discussed in [P2], [P3], [P4], and [P6]. Vortex dynamics in ^{3}He-B is discussed in [P7], [P8], [P9], [P10], [P11], [P12], and [P13].

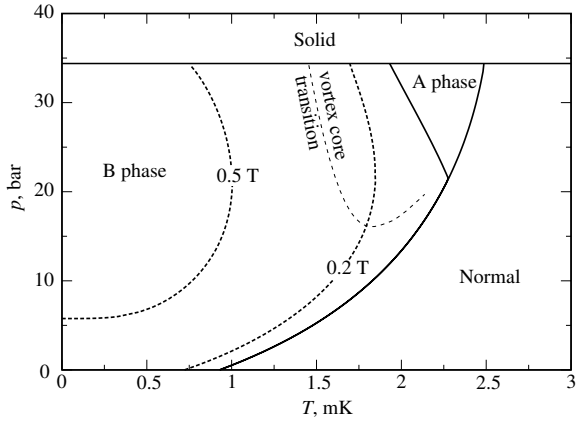

Figure 1: The phase diagram of liquid ^{3}He below 3 mK. ^{3}He liquifies at 3.2 K at atmospheric pressure. Far below the Fermi temperature $T_{\rm F} \approx 1$ K its properties are explained by the Fermi liquid theory [5]. The normal to superfluid transition at $T_{\rm c}$ is of second order while the AB transition is of first order. The A phase at zero external magnetic field occupies only a small part of the phase diagram. The external magnetic field makes the A phase more favorable. The dashed lines show where the A to B transition is located at two different magnetic fields. Above 0.6 $T_{\rm c}$ the A phase is stable at all pressures. The data for the AB transition are from Ref. [7]. The transition between the two vortex core types in ^{3}He-B is also shown [8].

1.1 Superfluid ^{3}He

The ^{3}He atom is a composite fermion with spin 1/2 and cannot undergo Bose-Einstein condensation. At low temperatures $T < 0.1$ K its properties follow the Fermi liquid theory [5]. The superfluidity emerges through Cooper pairing in a similar fashion as superconductivity appears in a superconductor, as explained by the BCS theory [6]. In a conventional superconductor, the electrons pair in the spin-singlet s-wave (S=0, L=0) state. In ^{3}He, the strongly repulsive interatomic potential at close range favors spin-triplet p-wave pairing (L=1, S=1) leading to a 3×3 complex order parameter matrix $A_{\mu j}$. The first index refers to spin and the second to orbital degrees of freedom.

There are three stable bulk phases in superfluid ^{3}He: A (sometimes referred to as A_2), B, and A_1. Fig. 1 shows the phase diagram. The two main bulk phases, ^{3}He-A and ^{3}He-B, are studied in this thesis. A_1 can only exist in the presence of large magnetic fields in a narrow temperature interval around the superfluid transition temperature at zero magnetic field.

The A phase corresponds to the Anderson-Brinkman-Morel (ABM) state [9]. Here the Cooper pairs are formed in the $S_z = \pm 1$ ($|\uparrow\uparrow\rangle$ and $|\downarrow\downarrow\rangle$) states.

The order parameter in ^{3}He-A is

$$A_{\mu j} = \Delta_0 d_\mu (m_j + i n_j), \tag{1}$$

where $\hat{\mathbf{n}} \perp \hat{\mathbf{m}}$. Vector $\hat{\mathbf{l}} = \hat{\mathbf{m}} \times \hat{\mathbf{n}}$ is in the direction of the angular momentum of the Cooper pair and $\hat{\mathbf{d}}$ is the unit vector in the direction where the projection of the spins disappears. Δ_0 is the maximum energy gap. In the A phase the gap is anisotropic such that it vanishes at two point nodes along $\hat{\mathbf{l}}$.

There are several competing forces trying to orient $\hat{\mathbf{l}}$ and $\hat{\mathbf{d}}$ in ^{3}He-A. The spatial variation of the anisotropy vectors is called the texture. The bending or gradient energy favors a uniform texture, the minimum local distortions in the $\hat{\mathbf{l}}(\mathbf{r})$ and $\hat{\mathbf{d}}(\mathbf{r})$ vector fields. The strength of other orienting forces can be characterized by their respective healing lengths. A healing length is obtained by equating the energy density associated with a particular orienting force to the bending energy density. The dipole interaction between the nuclear spins prefers to align $\hat{\mathbf{l}} \parallel \hat{\mathbf{d}}$. The healing length for the dipolar interaction $\xi_{\mathrm{D}} \sim 10$ μm. The preferred orientation of $\hat{\mathbf{d}}$ in the presence of a magnetic field is $\hat{\mathbf{d}} \perp \mathbf{H}$. The magnetic healing length $\xi_{\mathrm{H}} \propto H^{-1}$. The field where $\xi_{\mathrm{D}} = \xi_{\mathrm{H}}$ is called the dipolar field $H_D \sim 3$ mT. At fields higher than H_{D} the applied magnetic field overcomes the dipolar interaction. The texture may become partly dipole unlocked: there may be regions where $\hat{\mathbf{l}}$ and $\hat{\mathbf{d}}$ are not parallel and the spin-orbit interaction is not minimized. In our experiments $H \gg H_{\mathrm{D}}$. Then the magnetic field fixes $\hat{\mathbf{d}}$ into one plain perpendicular to $\mathbf{H}$ where $\hat{\mathbf{d}}(\mathbf{r})$ is relatively homogenous. In most parts of the texture the $\hat{\mathbf{l}}$-field is dipole-locked to the $\hat{\mathbf{d}}$-field except for instance in soft cores of defects. In addition, $\hat{\mathbf{l}}$ is oriented perpendicular to the walls and at the AB phase boundary it is oriented parallel to the interface [10].

The dominant phase at low magnetic field is ^{3}He-B. It corresponds to the Balian-Werthamer (BW) state [11]. Here all the spin states $\mathrm{S_z} = 0, \pm 1$ are present in equal admixture among Cooper pairs. The order parameter is

$$A_{\mu j} = \Delta e^{i\varphi} \mathbf{R}_{\mu j}(\hat{\mathbf{n}}, \Theta), \tag{2}$$

where φ is an overall phase factor and $\mathbf{R}(\hat{\mathbf{n}}, \boldsymbol{\Theta})$ is a rotation matrix describing the relative orientation of the spin and orbital spaces. Here $\hat{\mathbf{n}}$ denotes the axis of rotation and Θ is the rotation angle. Its value is fixed by the dipolar interactions to $\Theta = \arccos(-1/4)$ in equilibrium. The texture is formed from the spatial variation in the orientation of the symmetry axis $\hat{\mathbf{n}}(\mathbf{r})$. The magnetic healing length in the B phase is rather long, $\xi_{\mathrm{H}} \sim 1$ mm, in typical experimental conditions. The energy gap Δ is isotropic at zero field but gets distorted at higher fields. Most of the NMR measurements in this thesis concern the B-phase.

1.2 Vortex lines in ^{3}He-B

At steady state conditions the condensate of He-II can be described by a wave function of the form $\psi(\mathbf{r}) = \psi_0(\mathbf{r})e^{i\phi(\mathbf{r})}$ where ψ_0 is the amplitude and ϕ is a real function indicating the phase. The superfluid velocity is proportional to the gradient of the phase as $\mathbf{v}_\mathrm{s} = \frac{\hbar}{m_4}\nabla\phi$. From this definition it is seen that $\nabla\times\mathbf{v}_\mathrm{s} = 0$ - the superfluid as such is irrotational. Furthermore, since the wave function is single valued, a trip around a region where the order parameter vanishes must leave it unchanged i.e. ϕ varies as a multiple of 2π: The circulation is quantized.

The classic experiments by Osborne [12] showed that the surface of He-II, rotating at constant Ω, is concave as if it was a regular viscous liquid. Somehow the superfluid fraction must rotate along with the container. It turned out [13, 14] that the superfluid mimics solid-body rotation because of the presence of quantized vortex lines, each carrying one quantum of circulation $\kappa = h/m_4 = 0.0998$ mm^2/s. Rotation for a superfluid is analogous to the application of a magnetic field on a type-II superconductor where the magnetic field may penetrate the superconductor in the form of quantized vortex lines. In He-II vortex lines have a singular core with a diameter comparable to the coherence length $\xi \sim 0.1$ nm [15] which is of atomic size. A vortex line is a topologically stable object, it cannot end in the middle of the condensate - it either forms a loop or ends at the walls.

Superfluid ^{3}He-B is in many ways similar to He-II. The superfluid velocity is given by

$$\mathbf{v}_\mathrm{s} = \frac{\hbar}{2m_3}\nabla\varphi, \tag{3}$$

where m_3 is the mass of a ^{3}He atom. As in He-II, there is an explicit phase factor φ in the order parameter. Vorticity in ^{3}He-B resembles the conventional vorticity found in superconductors or in He-II. The quantum of circulation $\kappa = \frac{h}{2m_3}$=0.066 mm^2/s. In ^{3}He-B the vortices have a superfluid hard core where the order parameter deviates strongly from the bulk. However, the core is not singular (the order parameter does not vanish in the center of the core). The core radius is of the order of the coherence length $\xi(P,T) \sim 10$ nm. Depending on temperature and pressure there exist two types of vortex cores in ^{3}He-B, the axisymmetric and non-axisymmetric [16]. At 29.3 bar the transition between these two vortex structures occurs at 0.60 T_c (see Fig. 1). At lower pressure the non-axisymmetric vortex becomes the dominant structure and below 15 bar there is no transition. (Also a third vortex core structure exists, the spin mass vortex [17] but is not relevant in these measurements.)

1.3 Vortex lines in ^{3}He-A

In the A-phase the situation is not as straightforward since according to the Mermin-Ho equation [18]

$$\nabla \times \mathbf{v}_\mathrm{s} = \frac{\hbar}{4m} \sum_{ijk} \epsilon_{ijk} \hat{l}_i (\nabla \hat{l}_j \times \nabla \hat{l}_k) \tag{4}$$

does not necessarily vanish in an inhomogeneous order parameter field $\hat{\mathbf{l}}(\mathbf{r})$. We note from Eq. (4) that if $\hat{\mathbf{l}}$ is confined to vary in one plain then $\nabla \times \mathbf{v}_\mathrm{s} = 0$, but in a 3-dimensional case this need not be the case. It turns out, that in typical experiments boundary conditions, the bending energy, and the $\hat{\mathbf{d}}$-field influence the $\hat{\mathbf{l}}$-field such that flow is quantized also in the A phase [19].

The order parameter in ^{3}He-A allows a large variety of topological defects. In the experiments described in this thesis the magnetic field is always sufficiently high that it fixes $\hat{\mathbf{d}} \perp \mathbf{H} \parallel \boldsymbol{\Omega}$ which limits the number of relevant vortex structures to three [20].

The most important regarding this work is the double-quantum vortex (DQV) [21] which is the dominant structure in most of the experiments described here. It is a continuous vortex, which means that $\hat{\mathbf{l}}$ varies smoothly over the entire cross section of the vortex line [18]. To accomplish this the $\hat{\mathbf{n}}$ and $\hat{\mathbf{m}}$ vectors wind twice around $\hat{\mathbf{l}}$, leading to double quantization. Its structure consists of two Mermin-Ho vortices or merons. The length scale of these dipole uncoupled structures is set by the healing length of the spin-orbit interaction $\xi_\mathrm{D} \sim 10$ μm since in the vortex core $\hat{\mathbf{l}}$ deviates from the almost homogenous $\hat{\mathbf{d}}$ orientation. Compared to vortex lines in ^{3}He-B, the core here is three orders of magnitude larger.

The two other types of vorticity in the A phase relevant to this thesis are the vortex sheet (VS) [22] and the single-quantum vortex line (SQV). In a vortex sheet the merons form a double quantum vortex and are bound to a soliton-like domain boundary and form a sheet-like structure. The energy barrier to form a DQV is lower than that of the VS. However, once a sheet is present in the sample new vorticity can enter easily where the soliton connects to the walls since the order parameter is already distorted there. In the experiment, a vortex sheet can be formed in an oscillatory rotation.

The single-quantum vortex line has a nonsingular hard core (radius $\sim \xi$). The hard core in the $\hat{\mathbf{l}}$ texture is required by the boundary conditions but the vorticity is formed by the large soft core $\sim \xi_\mathrm{D}$ surrounding the hard core. The SQV is energetically favorable to the DQV at low rotation but it has a higher critical velocity of formation. Typically in rotation experiments it is only observed when the sample is cooled through T_c at low rotation. In these experiments the singly quantized lines are created when the sample is cooled under rotation through T_c [P3].

1.4 Two-fluid model and mutual friction

The two-fluid model is a phenomenological description of a superfluid [23]. The liquid is divided into normal and superfluid components. The normal component behaves like a regular viscous liquid while the superfluid component is an ideal inviscid superfluid where vorticity appears as quantized vortex lines. The total density ρ is divided such that $\rho = \rho_\mathrm{n} + \rho_\mathrm{s}$ where ρ_n and ρ_s are the densities of the normal and superfluid components and the total mass current is given by $\mathbf{j} = \rho_\mathrm{n}\mathbf{v}_\mathrm{n} + \rho_\mathrm{s}\mathbf{v}_\mathrm{s}$.

Mutual friction describes the interaction between the normal and superfluid components. The interaction is mediated by vortex lines. The velocity $\mathbf{v}_\mathrm{L}$ at which a segment of vortex lines moves in the flow is [24]

$$\mathbf{v}_\mathrm{L} = \mathbf{v}_\mathrm{s} + \alpha\hat{\mathbf{s}} \times (\mathbf{v}_\mathrm{n} - \mathbf{v}_\mathbf{s}) - \alpha'\hat{\mathbf{s}} \times [\hat{\mathbf{s}} \times (\mathbf{v}_\mathrm{n} - \mathbf{v}_\mathrm{s})]. \tag{5}$$

Here $\mathbf{v}_\mathrm{n}$ and $\mathbf{v}_\mathrm{s}$ are the local velocities of the normal and superfluid components at the position of the vortex segment, and $\hat{\mathbf{s}}$ is the unit vector along the vortex, α and α' are the temperature and pressure dependent mutual friction coefficients which describe how the vortex lines interact with the normal component. For ^{3}He-B they were measured in Refs. [25, 26] and calculated in Ref. [27]. Hydrodynamic data for ^{4}He can be found in Ref. [28].

In the typical experimental temperatures in each liquid the mutual friction in He-II is much smaller than either in the A or the B phase of ^{3}He. Figure 2 shows values of the mutual friction coefficients α and $(1-\alpha')/\alpha$ for ^{3}He-B and He-II for comparison. In the case of A phase the friction is very high and the effects described later as turbulent vortex flow are not visible in the currently achievable temperature regime.

A vortex line can support helical Kelvin waves. They are excited as a result of disturbances such as reconnections [29] or in the Kelvin wave instability [30, 31] when a sufficiently large flow of the normal component is present parallel to the vortex segment. The propagation of Kelvin waves is damped by mutual friction. At high temperatures when $\alpha > 1$ the waves are over-damped. Kelvin waves are expected to play an important role in superfluid turbulence, discussed in Sec. 4.

Since the normal component exerts a drag on the vortex lines, its properties are important in vortex dynamics. According to the Fermi liquid theory the viscosity of the normal component is $\propto T^{-2}$. Close to the superfluid transition at melting pressure the viscosity is $\eta = 12.5 \cdot 10^{-3}$ kg/ms [32]. The kinematic viscosity $\nu = \eta/\rho$ is a more useful quantity for describing fluid motion and for ^{3}He $\nu = 1.1 \cdot 10^{-4}$ m^2/s which is comparable to olive oil at 70°C. In our experiments the high viscosity of ^{3}He clamps the normal component to move with the container. In contrast, the normal ^{4}He is one of the least viscous fluids around. Its kinematic viscosity is orders of magnitude lower, $\nu \sim 10^{-8}$m^2/s.

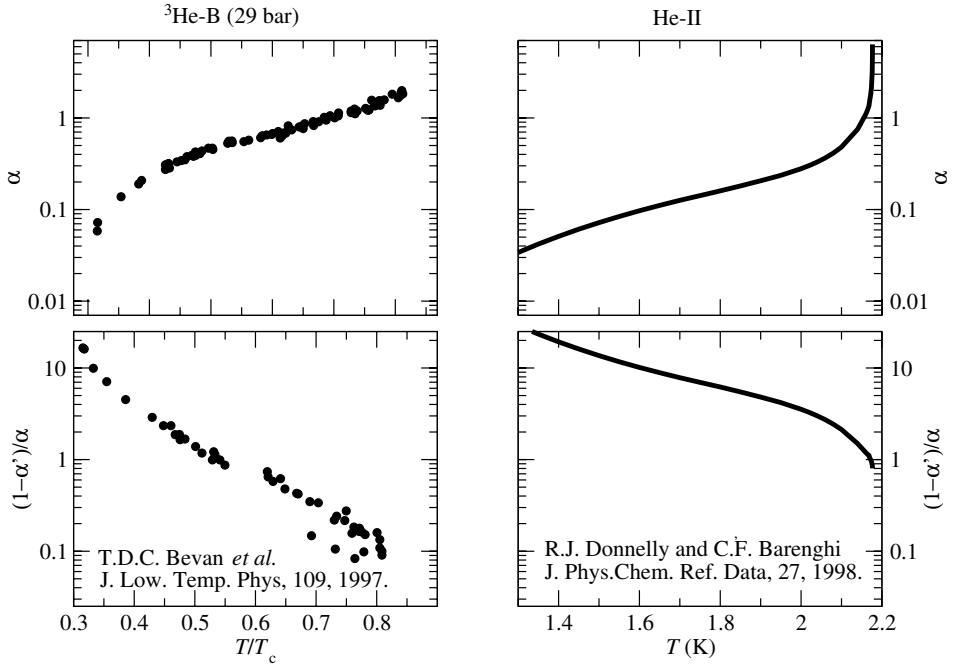

Figure 2: The mutual friction coefficients in ^{3}He-B (*Left*) and He-II (*Right*). The data for ^{3}He-B is from Refs. [25, 26] and for He-II from Ref. [28].

1.5 Superfluid under rotation

If the superfluid is set in rotation at constant angular velocity the normal component behaves like a normal liquid and rotates (eventually) along with the container. This is called solid body rotation and in this state $\nabla \times \mathbf{v}_\mathrm{n} = 2\Omega$. The superfluid component will remain stationary in the inertial coordinates if there are no vortex lines. The velocity difference between the normal and superfluid components is called the counterflow. The vortex-free state is the maximum energy state where it is favorable to form vortex lines and thereby reduce the counterflow. The minimum velocity when it becomes favorable to have the first vortex in a rotating container is the Feynman velocity $\Omega_{c1} = \frac{\kappa}{2\pi R^2} \ln(R/a)$, where a is the radius of the vortex core usually of the order of the coherence length ξ. For a R=3 mm container the limit is already at a rotation speed of $\Omega_{c1} \sim 0.01$ rad/s in ^{3}He-B. However, it is possible to maintain vortex free flow up to two orders of magnitude higher velocities since there is an energy barrier preventing vortex formation. In rotation the equilibrium configuration of a vortex is a rectilinear line parallel to the rotation axis. When several vortex lines are present, these form a cluster in the center of the rotating sample. Within this cluster the areal density of the rectilinear vortex lines is $n = \frac{2\Omega}{\kappa}$ and the superfluid component

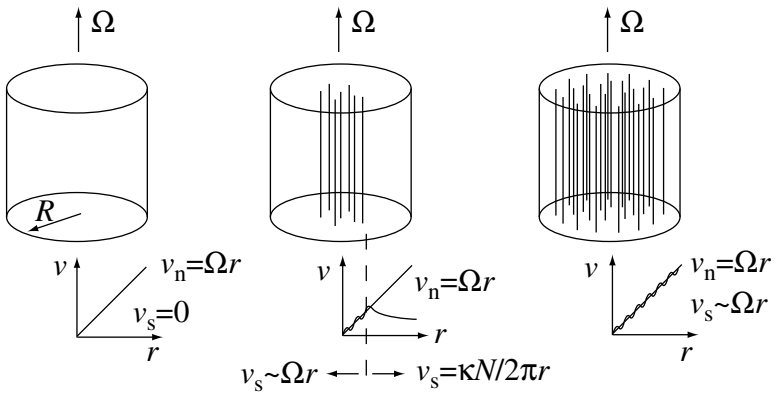

Figure 3: (*Left*) Vortex-free state; the superfluid component is at rest and the normal component rotates with the container. (*Center*) When $0 < N < N_{\rm eq}$ the superfluid mimics solid body rotation in the cluster while outside one has the counterflow at the velocity $v_{\rm cf}(r) = \Omega r - \kappa N/2\pi r$. (*Right*) Equilibrium number of vortex lines: The superfluid follows on average the normal component. The case with no vortex lines is the maximum energy state and the minimum energy state is the case with the equilibrium number of vortex lines.

mimics solid body rotation $\nabla \times \langle \mathbf{v_s} \rangle = 2\mathbf{\Omega}$. The cluster may have any number of lines within the range $0 \leq N \leq N_{\rm eq}$, where $N_{\rm eq}$ is the equilibrium number of vortex lines. Then the superfluid is on the average in solid-body rotation which is the minimum energy state. Figure 3 summarizes the vortex configurations.

The differences in the structure of vortex lines are reflected in their critical velocities when the energy barrier is overcome and vortex lines are formed [33]. An order of magnitude estimate can be obtained by comparing the energy of a minimal vortex loop of the size of the vortex core $E_{\rm vortex} \sim \rho_{\rm s}\kappa^2\xi$ to the energy of the superflow in the volume of the loop $E_{\rm flow} \sim \rho_{\rm s} v_{\rm s}^2 \xi^3$ assuming vortex core radius $a \sim \xi$, where ξ is the coherence length of the superfluid state. The critical velocity above which it is possible to form a vortex is then $v_{\rm s} \sim \kappa/\xi$.

In He-II with $\xi \sim 1$ Å this critical flow velocity is the highest of the three superfluids. However, it appears that some number of remanent vortex lines are always present in He-II [34] which act as seed for the formation of new vortices. Once a small (but still with size $\gg \xi$) vortex segment is present, it starts to expand during increasing flow. According to our findings in ^{3}He-B one remanent line suffices to produce the equilibrium number of vortex lines through reconnection mechanisms [P12].

In ^{3}He-B the energy barrier $\sim 10^4$ K is three orders of magnitude higher

than in He-II. In addition, the temperature is three orders of magnitude lower $T \sim 10^{-3}$ K. In practice the barrier is overcome only by increasing the flow such that the barrier height approaches zero and the vortices are formed by an instability. In He-II the situation is different since the energy barrier ~ 10 K and $T_\lambda \sim 1$ K. If the temperature is not too low, thermal fluctuations are expected to assist in the process [35]. In the A phase the core size of the DQV is of the order of $\xi_{\rm D} \sim 10$ μm and the velocity required for its formation is low. In these experiments vortex lines enter the A phase already at around 0.1 rad/s rotation.

1.6 NMR

Our superfluid sample is probed with NMR (nuclear magnetic resonance). A nucleus with a non-zero nuclear magnetic moment can be excited to resonance in a magnetic field $\mathbf{H}$ with rf excitation at a frequency $\omega_0 = \gamma H$. Here γ is the gyromagnetic ratio, which for the ^{3}He nucleus is $\gamma/2\pi = 32.4 \cdot 10^6$ Hz/T.

Leggett worked out the theoretical basis for understanding the NMR line shape in the superfluid phases of ^{3}He and wrote down the famous Leggett equations [36]:

$$\dot{\mathbf{S}} = \gamma \mathbf{S} \times \mathbf{H} + \mathbf{R}_{\rm D} \tag{6}$$

$$\dot{\mathbf{d}} = \mathbf{d} \times \gamma (H - \frac{\gamma}{\chi} \mathbf{S}) \tag{7}$$

where $\mathbf{R}_{\rm D}$ is the dipole torque on $\mathbf{S}$ which originates from the spin-orbit interaction. Since $\mathbf{R}_{\rm D}$ depends on the order parameter, the texture can be probed using NMR.

In this thesis most NMR measurements concern the B phase. The measurements are done using cw-NMR (continuous wave NMR). Discussion on the cw-NMR spectra in the A phase can be found for example in Refs. [37, 38], here we concentrate on the B-phase spectra. Some examples of the spectra, with varying numbers of vortex lines are shown in Fig. 4. These spectra are formed through the influence of the $\hat{\mathbf{n}}$ texture on the resonance frequency.

In the high field limit ($H \gg 2.5$ mT) relevant to this work, the resonance frequency depends on the angle β between $\mathbf{H}$ and $\hat{\mathbf{n}}$ approximately as [39]

$$\omega = \omega_0 + \frac{\Omega_{\rm B}^2}{2\omega_0} \sin^2 \beta, \tag{8}$$

where $\Omega_{\rm B}(P,T)$ is the Leggett frequency in ^{3}He-B and $\omega_0 = \gamma H$ the Larmor frequency. In the local oscillator model, the total spectrum is the sum of the contributions at different inclination angle β integrated over the volume of the sample.

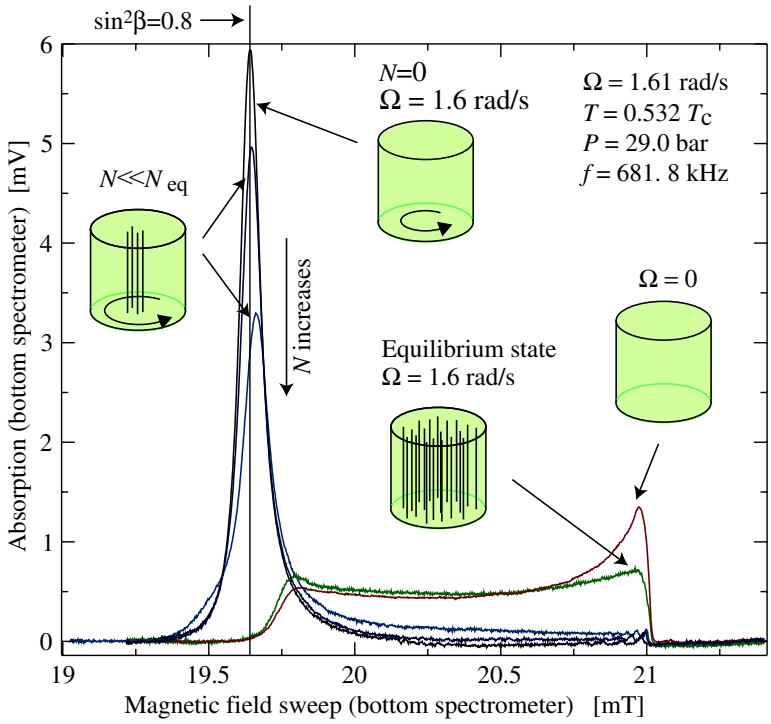

Figure 4: Examples of B-phase spectra at different rotation velocities and the dependence of the lineshape on the number of vortex lines. In our measurements the excitation frequency is kept constant and the magnetic field is swept over the spectrum. The Larmor value is about 21 mT in these measurements. The large peak on the left is the counterflow peak at $\sin^2\beta = 0.8$. Its amplitude reduces rapidly with increasing number of vortex lines.

The following effects are most relevant to the lineshape of the NMR spectrum: In the B phase the magnetic field tends to orient $\hat{\mathbf{n}}$ parallel to itself. In the bulk, at the center of the cylinder (assuming $\xi_{\rm H} < R$), $\hat{\mathbf{n}} \parallel \hat{\mathbf{H}}$ i.e. $\beta = 0$ and there is no frequency shift - absorption is at the Larmor frequency. Close to the cylinder wall there is a preferred orientation of $\hat{\mathbf{n}}$ such that $\hat{\mathbf{n}}$ makes an angle $\beta = 63.4°$ with the magnetic field and the axis of the cylinder. Here $\sin^2\beta = 0.8$ and the absorption is at a shifted frequency according to Eq. (8), which in this case happens to be the maximum shift. Overall the $\hat{\mathbf{n}}(\mathbf{r})$ field forms a continuous distribution known as the flare-out texture [40, 41] in a cylinder.

In a rotating sample the counterflow tends to align $\hat{\mathbf{n}}$ at $\sin^2\beta = 0.8$. This is the same value of β as that preferred at the wall parallel to the magnetic field. However, the optimum azimuthal angle differs by 90° in these

two cases. When the counterflow is increased a prominent peak (counterflow peak) appears. The competing orientational forces with respect to the azimuthal angle leads to a sequence of textural transitions when the vortex free sample is studied as a function of increasing flow velocity [42].

The observation of vortex lines in the B phase is based on their effect on the global counterflow. Vortex lines reduce the flow and absorption is shifted from the counterflow peak at $\sin^2\beta = 0.8$ closer to the Larmor frequency. In the NMR signal this is seen as a step-like increase in the absorption in the Larmor region or as a decrease in the counterflow peak height. In Fig. 7, such discontinuous absorption changes are illustrated by the ascending staircase pattern, which is recorded in the Larmor region. With current NMR methods it is possible to resolve the effect of a single vortex line [43] on the spectrum at $T \gtrsim 0.8\ T_{\rm c}$. The absorption change per vortex line can be calibrated by various experimental procedures. In some cases the line shape has been calculated numerically [39] to compare with the experimental data.

The temperature dependent Leggett frequency $\Omega_{\rm B}(P,T)$ can be used as a thermometer [44] since $\sin^2\beta = 0.8$ in the spectra is easily identifiable either from the counterflow peak under rotation or the cutoff of the spectrum at $\Omega = 0$. This method has the clear advantage that the temperature of the sample itself is directly measured.

2 Experimental setup

2.1 The ROTA cryostat

The experiments in this thesis were carried out in a rotating cryostat [45]. When the ROTA cryostat became operational in 1981, it was the first and for many years the only one capable of reaching the temperatures required for superfluid ^{3}He experiments under rotation. The first observations on quantized vortices in ^{3}He were produced here and published in 1982 [19].

Multiple cooling stages are needed in order to reach the temperatures required for superfluid ^{3}He. The most important of these are the dilution refrigerator and the nuclear demagnetization cooling stage [46]. The ^{3}He-^{4}He dilution machine precools the nuclear demagnetization stage. The best dilution machines achieve temperatures of a few mK. This is not low enough to cover all of the superfluid ^{3}He phase diagram. Therefore, adiabatic nuclear demagnetization is used for cooling the sample further to the target temperature of the experiment.

The ROTA cryostat is floating on air bearings in order to provide smooth rotation. In the experiments described here the maximum angular rotation velocity was 3.7 rad/s. The cryostat has torsional resonances which are seen as small oscillations in the rotation speed. For some experiments this is a handicap. For example, if the NMR spectrum is dependent on rotation speed, variations in speed are directly translated to noise in the NMR absorption amplitude [P5].

After the present experiments the old setup was disassembled and a new dilution machine was installed in place. The goal is to achieve lower temperatures, increase the duration of the measurement session from 12 h, improve the quality of the rotation, and increase the overall reliability of the rotating refrigeration installation.

2.2 Experimental arrangement

The superfluid ^{3}He sample is contained in a high quality fused quartz tube. Smoothness of the surface and its cleanliness have turned out to be the most important properties. To give an example, the same experimental container was used twice in two separate cooldowns but cleaned in between. It showed very different characteristics of vortex formation. In the first attempt the highest velocity of vortex-free rotation was around 2 rad/s. Later, after careful cleaning of the sample chamber, the critical velocities at $T < 0.8\ T_c$ were higher than the cryostat could achieve.

The principle and scheme of the cw-NMR spectrometer is described in Fig. 6. The detector is a superconducting coil connected to a low-loss capacitor forming a parallel LC resonator. In the NMR experiment the ^{3}He

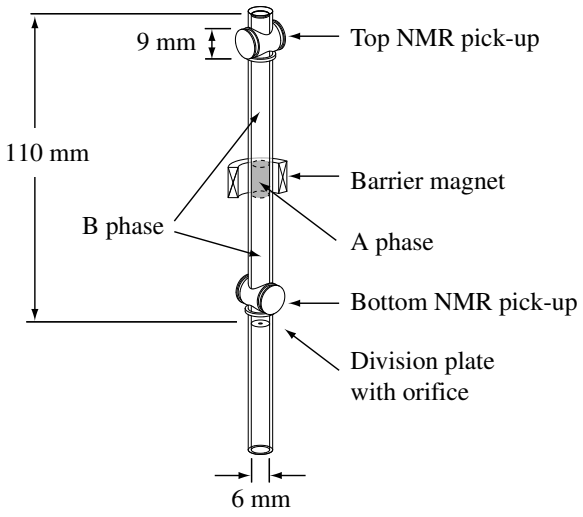

Figure 5: The measurement setup. The superfluid ^{3}He sample is contained in a high quality quartz cylinder. The ^{3}He in the experimental volume is connected through a small hole in a division plate to the heat exchanger volume. The division plate is needed to prevent vortex lines from migrating to the sample from the heat exchanger volume. NMR pick-up coils are placed close to both ends of the sample volume. Two magnets with homogenous axial fields provide the polarizing fields for the two NMR spectrometers. A third magnet (barrier magnet) is used to stabilize the A phase in the middle of the sample.

sample changes the unloaded inductance L_0 of the pick-up coil as

$$L = L_0(1 - \zeta\chi(\omega)), \tag{9}$$

where $\chi(\omega) = \chi'(\omega) - i\chi''(\omega)$ is the susceptibility and ζ the filling factor, an indication how large a proportion of the volume inside the coil is filled with the sample. As the externally applied magnetic field is swept, the sample goes through resonance and χ changes. A merit of quality for oscillators is the so called Q value. It is defined as

$$Q = \omega \frac{\text{stored energy}}{\text{dissipated power}}. \tag{10}$$

Since the absorption caused by the sample is in parallel to other intrinsic loss mechanisms in the resonator, the larger the Q the larger in proportion is the effect of the sample on the resonator. Thus high Q is desirable. The Q values of the resonators in these experiments have been 11000 in the top and 9000 in the bottom spectrometer.

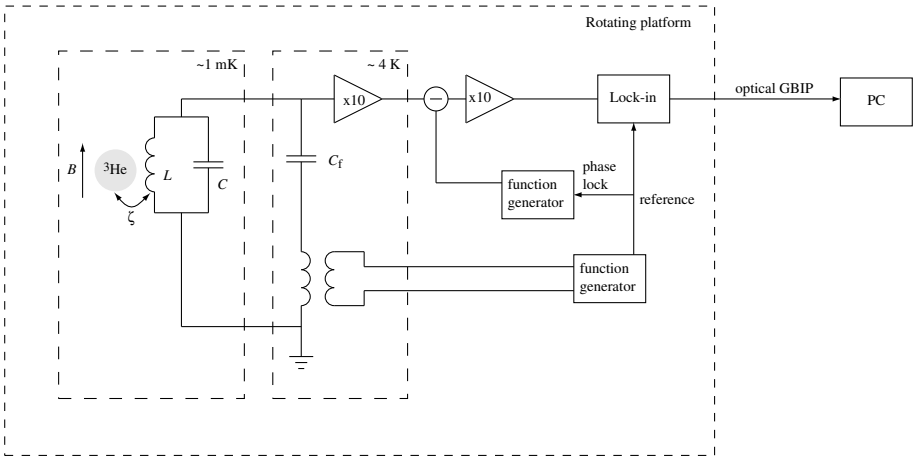

Figure 6: Main components of the measurement setup. The superfluid ^{3}He sample is probed with a high-Q LC resonator. The principle of this NMR spectrometer is that of a Q-meter, where the dissipation on a LC-resonator is monitored [48]. The high input impedance cryogenic preamplifier [49] is operated at liquid helium temperature. The two function generators (model HP 33120A) are coupled with variable phase shift and amplitude. The first provides the excitation to the sample and the second is used to compensate the signal passing the NMR system in the absence of the resonance in the sample (signals are subtracted in Stanford Research Systems SR560 differential preamplifier) before the signal is read with a lock-in amplifier (Stanford Research Systems model SR844). The data is read out and the devices are controlled through a GBIP bus.

The resistive losses in the superconducting circuit are vanishingly small and the high-Q capacitors [47] in our setup have small dielectric losses compared to other loss mechanisms. In our case, the most significant loss mechanism is radiation coupling to the external parts, and secondly the loading of the resonator by the preamplifier. The main function of the preamplifier is to decouple the resonator from the external circuitry at room temperature.

The coupling capacitor $C_{\rm f}$ and the LC resonator form a voltage divider which is fed through an input transformer and the output is read with a high-input impedance preamplifier at liquid helium temperature. The LC resonator has high impedance at resonance $z = Q\omega L$ and needs to be read out with a high input impedance preamplifier [49] not to load the Q of the resonator circuit. To minimize disturbances the preamplifier is situated at 4 K level inside the vacuum jacket.

The ^{3}He sample is tuned to resonance by sweeping the magnetic field. On resonance L changes and the voltage across the LC resonator drops. In this scheme the NMR signal is superposed on top of a large carrier signal.

A second function generator and a differential amplifier are used to subtract the carrier signal before the NMR absorption and dispersion envelope is read with a lock-in amplifier.

The detector coils are typically made from thin (25-50 μm) superconducting wire wound on a quartz bobbin. The presence of normal metals has proven to reduce the Q value [50], but a reliable non-ohmic contact to a thin niobium wire is difficult to prepare. In the end, 50 μm Cu/Ni coated Nb/Ti wire has turned out as most reliable since it can be soldered directly and is strong enough not to braek during cool down.

Because the tank circuit is one of the most critical parts in the spectrometer, a new approach for its construction was explored: The coil and the capacitor were fabricated out of niobium films on a single substrate. The planar coils were patterned to a 200 nm thick niobium film and the capacitor consists of two parallel niobium film insulated by 250 nm of SiO_2. The properties of such LC resonators were investigated in [P1]. There are a number of advantages in such a solid state device that one might expect: i) All the wires are permanently fixed in place. Movement of wires is a source of noise in the measurement (inductance and capacitance in the system changes). It would be especially advantageous to have both the coil and the capacitor on the same chip. ii) The coil can be made so that there are no regular conductors present. One observed source of loss is attributed to eddy current losses in normal conductors [50]. iii) The superconducting wire, because of the Meissner effect, distorts the magnetic field smearing the NMR spectrum. In a thin film device, the coil is only a few hundred nm thick, hundred times smaller than the thinnest regular wire at best, minimizing the field distortion. iv) The gyromagnetic ratio of hydrogen is relatively close to that of ^{3}He. The tail of this peak is seen as a sloping baseline on which the ^{3}He NMR signal appears. Hydrogen is present in glues, epoxy resins, wire insulation, etc. and with proper choice of materials this distortion can be minimized in a thin film device. A further goal is to miniaturize the detector coil to be used as a NMR microscope [51].

Planar sample coils were fabricated on silicon and sapphire substrates. The material of the substrate turned out not to have significance on the performance. The superconducting material was niobium and the SiO_2 insulation was deposited with PECVD (plasma enhanced chemical vapor deposition) technique [52]. The capacitors turned out to have a low Q value and were unstable in magnetic field. The planar coils tested by themselves with separate high quality capacitors showed high $Q \sim 10^5$, but displayed still traces of unstable behavior in magnetic field. In [P1] these problems were shown to be associated with the SiO_2 insulating layer. The PECVD fabrication results in amorphous material with various kinds of defects, impurities, and free radicals.

A set of planar coils which had only one layer of structured niobium film and no insulation was tested in the NMR setup of the ROTA cryostat

and used for NMR. In the experiment the coils performed similar to wire wound coils. The Q value was close the value of our typical wire-wound coils, presumably limited by the losses in the copper shield coating the bore of the magnet. However no great gain was achieved in the NMR field homogeneity. This probably means that it is primarily the polarizing magnets themselves which determine the homogeneity. Unfortunately, as such, the thin film devices are too cumbersome for practical use. In order to make these coils better than wire-wound ones, the problems with the insulation layer need to be solved. This is especially the case if the goal is to miniaturize for a NMR microscope [51].

The origin for the unstable properties of the SiO_2 insulation in low magnetic fields below 100 mK is an interesting problem in itself. To find out the source of the poor performance of the thin film resonators in magnetic field more tests are needed. One known problem with niobium rf cavities is the so called Q disease [53]. It is attributed to hydrogen forming hydrates during slow cool downs somewhere around 100 K. The SiO_2 insulation layer formed with PECVD is known to contain hydrogen but whether our problems are connected to the Q disease remain unanswered.

3 Shear flow instability of the AB interface

The original motivation for our experimental setup was to study what happens to topological defects on the phase boundary of two rotating quantum fluids. The dominating vortex structure in the A phase is the DQV. The large diameter of the vortex core is set by the dipolar coherence length $\xi_D \sim 10\ \mu$m which is reflected in the low velocity required for their formation. The B phase vortex has a hard core with a diameter comparable to the superfluid coherence length $\xi \sim 10$ nm and the critical velocity needed for their formation is much higher. What happens as the A phase starts to accumulate vorticity in increasing rotation? Do the vortex lines penetrate across the phase boundary from A to B phase or will the B phase remain vortex free? At the phase boundary superfluid coherence is preserved. This rules out the possibility that a vortex in the A phase would end at the boundary [10].

In earlier experiments the interaction of the AB interface and vortex lines [54] has been examined in situations where the AB interface was not stabilized. Instead, the AB interface moved through the sample such that the A phase was replaced with the B phase. Here, depending on the speed of the moving boundary, some vortex lines penetrated through the boundary to the B phase side while others were pushed away by the AB interface to the sample boundaries for annihilation, leaving a deficit of vortex lines in the B phase.

The experimental setup is described in Fig. 5. The A phase is stabilized with the barrier magnetic field. There are two possible configurations in which the AB phase boundary measurements can be carried out. In the first, the A phase is stabilized with high magnetic field in the middle and the upper and lower parts are stable B phase. Here, the upper and lower parts are identical and redundant. They are also independent of each other with respect to vortex formation which was shown in these experiments. In the second configuration there is stable B phase on the bottom, magnetically stabilized A phase in the center and supercooled A phase at the top. This configuration can be achieved by cooling down from the temperature where A phase is stable also at zero field. The A phase generally supercools quite substantially [55]. In the smooth-walled quartz container the A phase in our experiment can supercool to 0.52 T_c at 29 bar. In contrast, the heat exchanger has rough surfaces and here B phase nucleates easily. The bottom part of the container is in contact with the heat exchanger volume through the orifice and thus the B phase expands into this section after it has nucleated. The top, however, is shielded by the stable A-phase barrier in high magnetic field and does not react when B phase enters the bottom section. This configuration allows monitoring the vortices in the A phase with NMR.

When rotation is slowly increased from rest, vortex lines start to form in the A phase at around 0.1 rad/s. In other words the superfluid component

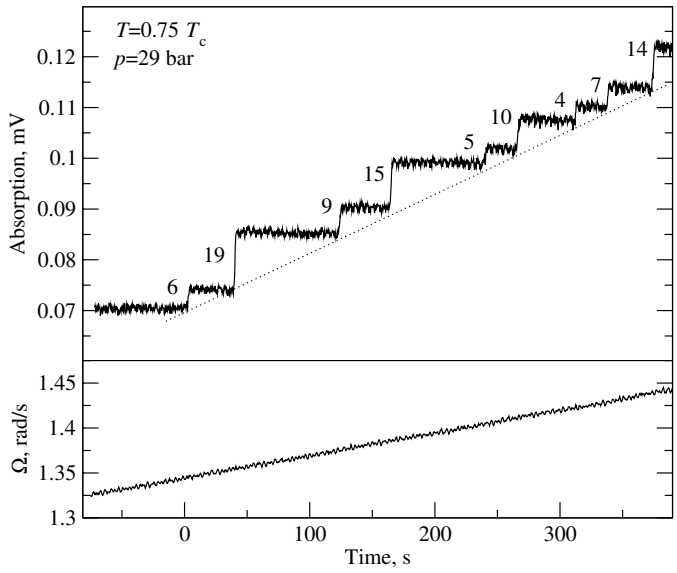

Figure 7: A series of instability events during a continuous increase of Ω. The boundary injects a small number of vortex lines each time the critical velocity is reached. The top graph shows the NMR absorption measured close to the Larmor frequency. Here the increasing number of rectilinear vortex lines in the B phase is shown as increased absorption. In the bottom panel the rotation velocity is shown. The number of vortex lines injected in each event in the B phase is indicated beside the step. A detailed analysis [P6] confirms that both even and odd numbers of vortex lines may be injected across the AB interface into the B phase despite the fact that the vortex lines in the A phase are doubly quantized.

in ^{3}He-A starts to rotate with the normal component on the average while at such low velocities the B phase stays vortex free $N_{\rm B} = 0$. This experiment showed that vortex lines form in the A phase but do not cross the AB interface until at some well-defined critical velocity a burst of vorticity penetrates across the boundary.

Once the rotation velocity reaches the critical limit for the stability of the AB interface, vortex lines are injected in the B phase, typically a few lines ($\Delta N_{\rm B} \sim 10$) per event. The sequence of injection events in Fig. 7 results from a continuous acceleration at constant rate. The increasing number of vortex lines $N_{\rm B}$ winds up the superfluid velocity in the B phase section, the counterflow velocity is reduced, and it becomes stable. During the continuous rotation acceleration in Fig. 7 the same critical counterflow velocity is reached repeatedly resulting in a sequence of vortex injections. This creates the staircase pattern in the NMR absorption.

It turned out that a perfect explanation for our experimental results is

given by the stability analysis of the interface. This analysis demonstrates the instability of the AB interface which is similar to the instability known in the literature of classical hydrodynamics as the Kelvin-Helmholtz (KH) instability. The instability is not a direct consequence from the vorticity accumulating on the AB interface. It is caused by the difference in flow velocities parallel to the interface in the A and B phases.

In Lord Kelvin's original treatise [56] he considered the case of two ideal inviscid liquid layers flowing with respect to each other tangential to their interface. Gravity acts as a stabilizing force when the denser liquid lies below the lighter one. When the relative speed of the liquids exceeds a critical value waves start to form on the interface. The examples of this effect in nature are countless although it is never seen in the purest form because of the viscosity of regular fluids. The most familiar case is the wave formation on water when a wind blows over the surface. Our measurement is the first demonstration of the KH instability in superfluids. A schematic illustration of the process in our system is shown in Fig. 8.

When two liquids (gases) are flowing with respect to each other the interface between them becomes unstable towards wave formation when

$$\frac{\rho_1\rho_2}{\rho_1+\rho_2}(v_2-v_1)^2 = 2\sqrt{\sigma F_{\rm g}}. \tag{11}$$

Here ρ_1 and ρ_2 are the densities and v_1 and v_2 the velocities of the two liquids, σ the surface tension of the interface, and $F_{\rm g}$ the restoring force (in this case gravitational force $F_{\rm g} = g(\rho_1 - \rho_2)$. This is known as the Kelvin-Helmholtz instability. In the classical cases there is always friction present because of viscosity and the instability in its purest form is not seen. Superfluids provide a way around the mathematical complexity introduced by viscous dissipation since they are inviscid. In a sense as long as we focus on the instability itself and do not worry about what happens later, we have here the ideal case to demonstrate the instability.

In the case of the A and B phases of superfluid ^{3}He the restoring force is of magnetic origin:

$$F_{\rm m} = \frac{1}{2}(\chi_{\rm A} - \chi_{\rm B})\nabla(H^2), \tag{12}$$

where $\chi_{\rm A}$ and $\chi_{\rm B}$ are the temperature and field dependent susceptibilities of the A and the B phases. The two-fluid hydrodynamics introduces modifications to the instability criterion since the normal component acts as a frame of reference. The criterion for the instability turns out to be [57] (neglecting the orbital anisotropy of ^{3}He-A)

$$\frac{1}{2}\rho_{\rm sA}(v_{\rm n}-v_{\rm sA})^2 + \frac{1}{2}\rho_{\rm sB}(v_{\rm n}-v_{\rm sB})^2 = \sqrt{\sigma_{\rm AB}F_{\rm m}}, \tag{13}$$

where $\rho_{\rm sA}$ and $\rho_{\rm sB}$ are the superfluid densities of the A and B phases, while $v_{\rm n}$ is the velocity of the normal component. In our case because of high viscosity

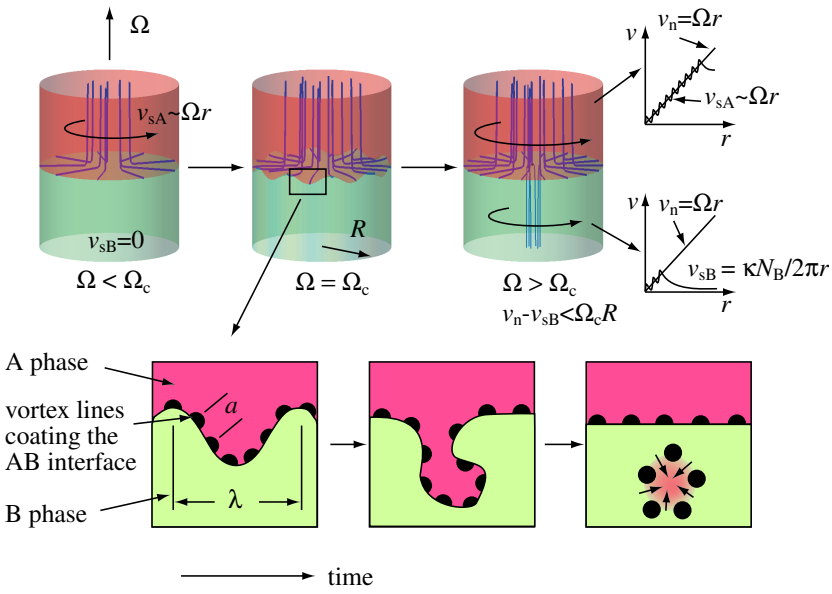

Figure 8: Schematic illustration of the shear-flow instability of the AB interface. During a slow increase of the rotation velocity the A and B phases behave differently. The A phase has a low critical velocity of vortex line formation. In continuous rotational acceleration the number of vortex lines $N_{\rm A}$ in the A phase increases and the superfluid fraction winds-up speed and rotates with the container. The B phase, however, remains vortex free and stays stationary in the laboratory frame. The AB phase boundary becomes unstable at some critical velocity difference $(v_{\rm s,B} - v_{\rm n})$ and a small number of vortex lines $\Delta N_{\rm B}$ is injected into the B phase. The velocities of the normal component and superfluid components in the two phases are sketched on the right (see also Fig. 3). A schematic illustration on how the vortex injection might happen is sketched below: As a result of the instability waves form on the AB interface and vortex lines become trapped in a corrugation. Below the interface A phase is unstable and shrinks away leaving the superfluid circulation behind. The vortex lines that enter the B phase in this way increase its velocity, the velocity difference across the boundary is reduced below the critical value and the boundary stabilizes. On increasing the rotation velocity further, the boundary becomes unstable again when the velocity difference has increased to the critical value.

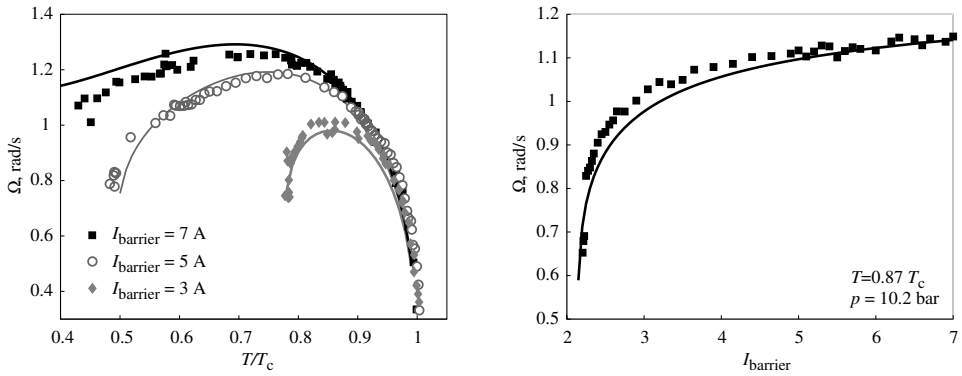

Figure 9: (*Left*) The dependence of the rotation velocity of the first vortex injection event (Ω_c) on temperature at three different values of the barrier magnet current at 10.2 bar pressure. (*Right*) Ω_c as a function of the current in the barrier magnet at fixed temperature of 0.87 T_c. The solid lines are theoretical predictions from Eq. (14) with no adjustable fitting parameters.

$\mathbf{v}_n = \mathbf{\Omega} \times \mathbf{r}$ ie. it follows the rotating cylinder. In addition, v_{sA} and v_{sB} are the superfluid velocities in the A and B phases, σ_{AB} is the surface tension of the phase boundary. In the classical case the velocity difference between the two fluids triggers the instability. In the superfluid the relative velocity difference between the normal component and the superfluid component produces the instability. It can be seen from Eq. (13) that the instability can happen even if both superfluid fractions are moving at the same speed. In this sense the phenomenon is similar to the classical and dissipative flapping flag instability, which was discussed by Raleigh (see for example Ref. [58] and references therein) but where the explanation of the instability is quite different.

In our experiment the instability is most practical to identify from the critical rotation velocity of the first vortex injection event at Ω_c. The A phase has always close to the equilibrium number of vortex lines. Thus $v_{sA} \approx v_n$. Before the instability at $\Omega < \Omega_c$ the B phase remains vortex free and $v_{sB} = 0$. The normal component rotates along with the container and at the outer wall its velocity is $v_n = \Omega R$. With these assumptions the instability criterion becomes

$$\Omega_c = \frac{1}{R}\left(\frac{4\sigma_{AB}(\chi_A - \chi_B)H_{AB}\frac{\partial H}{\partial z}|_{z(H=H_{AB})}}{\rho_s^2}\right)^{\frac{1}{4}}. \qquad (14)$$

Figure 9 displays the temperature dependence of Ω_c for the first vortex injection event at a few fixed values of the barrier field at 10.2 bar pressure (*Left*) and the field dependence at constant temperature (*Right*).

Theoretical values obtained from Eq. (14) are in good agreement. The parameters $\sigma_{\rm AB}$, $\chi_{\rm A}$, $\chi_{\rm B}$, $\rho_{\rm s}$, and $H_{\rm AB}$ can all be obtained from the literature. The surface tension $\sigma_{\rm AB}$ is measured in Ref. [59]. Since this value is for melting pressure we need to scale it to lower pressures using GL-theory. The susceptibility of the A phase is roughly the same as that of the normal phase [60]. The B phase susceptibility is reduced from the normal phase value [61]. The superfluid density in magnetic field is not well known, but here $\rho_{\rm s}$ at zero field is used [60]. H is $H_{\rm AB}$, the critical field of the AB transition measured in Ref. [7] and the field profile of the magnet gives the gradient at the location of the interface $\frac{\partial H}{\partial z}|_{z(H=H_{\rm AB})}$.

The instability develops with a wave length $\lambda = 2\pi\sqrt{\sigma_{\rm AB}/F_{\rm m}}$. The separation of the vortex quanta coating the AB interface is $a = \kappa/(v_{\rm sA} - v_{\rm sB})$. In one corrugation (half of the wave length λ) there are $\lambda/2a$ vortex quanta. Our measurements on the distribution of the number of vortex lines injected per event across the AB interface into the B phase are in reasonable agreement with the number of vortex lines expected to be in one corrugation [P10]. Furthermore, the number of injected vortex lines can be odd or even, despite the fact that the vortex lines in the A phase are doubly quantized. In [P6] it is shown that the doubly quantized vortex lines of the A phase separate to singly or half quantized units when they are confined to the AB phase interface.

The shear-flow instability is an interesting phenomenon for future study. Its properties at the lowest temperatures, when there is no normal component and no reference frame, is an open question. It also provided us with a convenient method for injecting vortex lines into originally vortex-free counterflow in ^{3}He-B. The key feature is that the velocity of injection can be tuned with the magnetic field. When the magnetic field is changed the phase boundary moves to a position such that the magnetic field has the critical value $H_{\rm AB}$ at the location of the phase boundary. Depending on the field profile, this results in a change in ∇H which changes the critical velocity in Eq. (14). The externally controllable injection velocity allows unprecedented flexibility in the study of vortex dynamics in ^{3}He-B.

4 Hydrodynamics of ^{3}He-B in rotation

4.1 Classical and quantum turbulence

Turbulence is a most common hydrodynamic phenomenon. Yet, it has turned out to be one of the most complicated problems in classical physics. As opposed to laminar flow, in turbulence fluid flow is characterized by the formation of eddies and their irregular motion. The larger eddies, limited by the size of the container, contain most of the kinetic energy. On this scale the viscous dissipation is small compared to the kinetic energy stored in the eddy. The energy is transferred in a cascade into smaller and smaller eddies until finally viscous dissipation starts to remove energy from the flow more efficiently. In the model case, to which many theoretical considerations refer, turbulence is considered to be homogenous and isotropic. In experiments, one realization is grid turbulence, where the fluid is pushed through a uniform grid. Mainly from dimensional arguments one deduces that the energy spectrum of fully developed homogenous and isotropic turbulence is of the form $E \propto \epsilon^{\frac{2}{3}} k^{-\frac{5}{3}}$, where k is the wave vector of the eddy and ϵ is the energy transfer rate. This is called the Kolmogorov law [62].

The starting point of the hydrodynamics of viscous flow is the Navier-Stokes equation,

$$\frac{\partial \mathbf{v}}{\partial t} + (\mathbf{v} \cdot \nabla)\mathbf{v} = \mathbf{F}/\rho - \nabla P/\rho + \nu \nabla^2 \mathbf{v}. \tag{15}$$

Here $\mathbf{F}$ is an external force per unit volume, P pressure, and ν the kinematic viscosity. In order to compare flows with different viscosities it is useful to write the Navier-Stokes equation in dimensionless units $x^0 = x/L$, $v^0 = v/V$ and $t^0 = Vt/L$, where L and V are characteristic values for length and velocity. The relative importance of the inertial term $\sim V^2/L$ and the viscous term $\sim \nu V/L^2$ in Eq. (15) can be used to characterize the flow. The ratio of these terms is a dimensionless quantity called the Reynolds number $Re = (V^2/L)/(\nu V/L^2) = VL/\nu$. For flows with small Re the dissipative forces are dominant and the flow is typically laminar. If Re is large, the inertial forces dominate and the flow usually turbulent [62].

Reynolds, after whom the similarity condition is named, was the first to conduct a systematic study on pipe flow. He found that intermittent bursts of turbulence become possible above $Re \approx 2000$. However, in carefully prepared experimental conditions where disturbances in the flow are minimized, laminar flows with very high Reynolds number have been recorded ($Re \approx 10^5$, [63]). However, with increasing Re the disturbance that is required to trigger turbulence decreases rapidly [64].

A superfluid, with its quantized vorticity and zero viscosity, opens up new possibilities in understanding turbulence. Since the flow is quantized, the minimum size of an eddy is one vortex, larger eddies need to be con-

structed as polarized arrays of several vortex lines. Vortex lines are topologically stable objects. They are continuous strings that either end at the boundary or form closed loops. Typically the intrinsic velocity needed for loop generation is high and is not exceeded in the usual experimental conditions. Rather, at low vortex damping the formation of new independent vortex lines is catalyzed by reconnections [65]. The existing lines may reconnect at walls or with other vortex lines (or themselves) and in the coarse of these processes form new loops. Similarly, a region of superfluid which is vortex-free will be filled with vortex lines only if they migrate there from other parts of the sample.

The first observations of phenomena related to superfluid turbulence are from thermal counterflow experiments in 1949 [66] but the explanation of these effects came later [67]. A large amount of experimental, theoretical, and numerical work has been done to explain superfluid turbulence in He-II. Experimental work on turbulence produced in a towed grid experiment in He-II points towards quasi-classical behavior [68, 69, 70, 71]. At higher temperatures mutual friction drags the normal and superfluid components into co-flow on length scales larger than inter-vortex spacing. Here, the Kolmogorov spectrum is present in both components. In the $T \rightarrow 0$ limit the normal component vanishes but the superfluid is still expected to have quasi-classical character on large length scales [71]. Unfortunately there are few experiments that investigate this regime. In Ref. [72] the drag force from He-II on a sphere is investigated at 25 mK. It appears to resemble the classical drag in the turbulent regime. In ^{3}He the combined turbulence of the normal and superfluid components becomes impossible because of the high viscosity of the normal component. Ideas in Refs. [73, 74] still support an energy cascade with dissipation at small length scales.

Prior to this work only measurements with a wire vibrating in stationary fluid have suggested the existence of turbulent vortex dynamics in ^{3}He-B: In Refs. [75, 76, 77] a turbulent vortex tangle is created with a vibrating wire resonator below 0.2 T_c where the normal component is expected to have a vanishing contribution. Reference [33] describes measurements in a rotating sample where vortex multiplication is observed. In many experiments carried out in this rotating cryostat prior to the ones described in this thesis, irregular vortex formation was found to be a serious nuisance at low temperatures hampering other experiments but its source was not carefully identified.

In these experiments we observe how vortex free ^{3}He-B, where the superfluid fraction is initially at rest in the laboratory frame, spins up to follow the rotation of the normal component. Although there is no classical analog to this experiment, some features are reminiscent of the spin-up process in a classical fluid [78, 79]. Our method of rotating the system provides a convenient way to study ^{3}He-B from the experimental point of view. However, rotation also imposes polarization on a vortex tangle. Thus, one needs to

be careful before comparing homogenous turbulence to that in rotation.

4.2 Turbulence in superfluid ^{3}He-B

Most experiments on quantum turbulence have been carried out in He-II. Much of this work is not possible to repeat in ^{3}He-B. Already the three orders of magnitude lower superfluid transition temperature limits the experiments that are possible. Some methods widely used for He-II such as thermal counterflow and vortex detection via the absorption of second sound are not suitable for ^{3}He. Still ^{3}He-B offers features that are instructive in the study of turbulence and which are not present in He-II: i) Vortex formation is under better control. ii) Viscosity of the normal component is high. iii) Mutual friction varies widely such that both laminar and turbulent behavior exist. iv) NMR provides a powerful tool for counting the number of vortices and mapping their patterns in rotating flow.

In ^{3}He-B, it is possible to create vortex free counterflow, which in He-II has turned out to be impossible in macroscopic-sized samples. The typical case in He-II is that there are always remanent vortex lines present [34]. The core radius of the vortex is of atomic scale $a \sim 0.1$ nm [15] and any solid surface on this scale is rough. For example, in experiments where He-II is rotated it has turned out that the sample is always close to the equilibrium vortex state. In ^{3}He-B the core size is larger $\sim 10 - 100$ nm and there is no evidence of pinning on carefully prepared surfaces. Not only high counterflow is possible, but also vortex lines can be introduced into vortex-free flow by means of externally controlled methods.

The viscosity of normal ^{4}He liquid is very small. In the experiments where superfluid turbulence is studied, also the normal component can be expected to be turbulent [70]. The case in ^{3}He-B is clear-cut with a four orders of magnitude higher viscosity of the normal component: In all practical cases in our experiment the normal component can be assumed to follow the container.

Although the superfluid component is inviscid, mutual friction damps the motion of vortex lines. One approach to look at the effect of mutual friction in superfluid dynamics is to write a coarse grained equation such that the superfluid velocity is averaged over volumes consisting of many roughly parallel vortex lines [80]. We characterize the flow with a "superfluid Reynolds number" $Re_\mathrm{s} = V_\mathrm{cf} L/\kappa$ where V_cf is the counterflow velocity. When $Re_\mathrm{s} \sim 1$, it is favorable to expand a vortex into the flow (Feynman criterion). Here, we now require $Re_\mathrm{s} \gg 1$. Assuming that the vorticity is locally polarized, the mutual friction force per unit volume of superfluid becomes [80]

$$\mathbf{F}_\mathrm{mf} = -\alpha\rho_\mathrm{s}\boldsymbol{\omega} \times [\hat{\boldsymbol{\omega}} \times (\mathbf{v}_\mathrm{n} - \mathbf{v}_\mathrm{s})] - \alpha'\rho_\mathrm{s}\boldsymbol{\omega} \times (\mathbf{v}_\mathrm{n} - \mathbf{v}_\mathrm{s}), \tag{16}$$

where $\boldsymbol{\omega} = \nabla \times \mathbf{v}$ is the (averaged) vorticity and $\hat{\boldsymbol{\omega}}$ is the unit vector in the

direction of $\boldsymbol{\omega}$. Assuming that the normal component is immobile due to its high viscosity we set $\mathbf{v}_{\rm n} = 0$. Since the superfluid component is inviscid, the Navier-Stokes Eq. (15) is simplified to the Euler equation which, assuming the force in Eq. 16, leads to a coarse-grained hydrodynamic equation [P7]

$$\frac{\partial \boldsymbol{\omega}_{\rm s}}{\partial t} = (1-\alpha')\nabla \times [\mathbf{v}_{\rm s} \times \boldsymbol{\omega}] + \alpha \nabla [\hat{\boldsymbol{\omega}} \times (\boldsymbol{\omega} \times \mathbf{v}_{\rm s})]. \qquad (17)$$

Similar dimensional analysis as in the case of the Navier-Stokes equation leads to new interpretation for the equivalent of the Reynolds number from Eq. (17). Here the inertial term $\sim (1-\alpha')V^2/L^2$ and the viscous term $\sim \alpha V^2/L^2$. Thus, their ratio $q^{-1} = (1-\alpha')/\alpha$. Analogously to the classical case Reynolds number we expect that q^{-1} can be used to characterize the flow: When q^{-1} is large the flow is dominantly turbulent and when q^{-1} is small the flow is laminar. Unlike the classical Reynolds number, q^{-1} is not dependent on the external variables L and V. The intrinsic properties of the fluid, α and α', determine whether turbulence is possible or not. Dimensional arguments on how the vortex length develops after vortex loops are injected lead to the same conclusion [81].

Judging from these arguments, He-II has in all experiments been far in the turbulent regime. Only if experiments in He-II were performed within a few μK below the λ-transition, would mutual friction be such that laminar behavior of vortex lines could be expected (see Fig. 2). Even then, the low-viscosity normal component would easily form turbulent flow patterns which the superfluid and vortex lines would follow. ^{3}He-B allows a study of the transition region $q^{-1} \sim 1$ in the superfluid component only, where the behavior changes from laminar to turbulent [P7]. Moreover, in ^{3}He-B the transition at $q^{-1} \sim 1$ appears in the middle of the accessible temperature range.

4.3 Vortex injection with the KH instability

The shear-flow instability of the AB phase boundary offers a practical tool to inject vortex lines into vortex-free counterflow because the flow velocity at which the injection occurs can be controlled externally with the magnetic field in the barrier magnet. The velocity range is 2-5 mm/s in the present experimental setup. In the simplest experimental procedure we prepare the vortex free rotating state, inject some vortex loops into the system, and record what happens (Fig. 10). In Fig. 11 we have calibrated the number of vortex lines in the final state as a function of temperature after vortex injection. The outcome, the number of vortex lines in the final state, after the system has stabilized, is recorded. A clear majority of the events fall into two categories: i) The number of vortex loops is close to the number of originally injected vortex lines, which is typical at high temperatures, while ii) at low temperatures the final state has close to the equilibrium number of vortex lines.

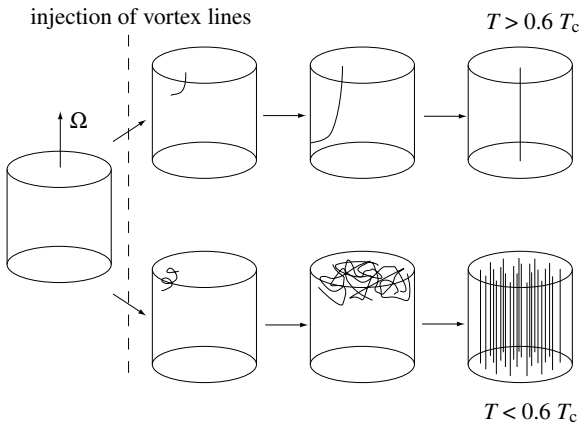

Figure 10: In an experiment where a small number of vortex lines is injected into superfluid flow the outcome depends on temperature (or mutual friction). It turns out that above 0.6 T_c an injected vortex line expands to its minimum energy state rapidly with no increase in the vortex number. Below this temperature curved vortex loops are unstable and typically rapid turbulent proliferation of vortex lines takes place. As a result the system ends up in its minimum energy state, the equilibrium vortex state. The experiment shows that rather than filling the whole cell with a vortex tangle, the turbulence develops rapidly as a localized burst. The vortex lines then propagate along the rotating column towards the vortex free counterflow as a front and leave behind the equilibrium number of vortex lines.

At high temperatures, the KH instability injects roughly 10 vortex loops per event into the B phase sections of the sample. The distribution of the number of injected loops was checked at 0.78 T_c in [P10]. There is no reason to expect that the number of originally injected loops would change dramatically as a function of temperature. Rather, at low temperature, the high number of vortex lines in Fig. 11 must be the result of a burst of turbulent vortex multiplication. It is evident from our data that there are very few cases where the turbulent multiplication ends at relatively low vortex numbers. Instead, it appears that once turbulence starts, it produces close to the equilibrium number of vortex lines in the final state. However, when the rotation velocity is slowly increased such that a sequence of vortex injection events occurs (as in Fig. 7) it is possible, especially in the transition regime, to have one or a few vortex injection events which do not lead to the turbulent multiplication before the injection which triggers the turbulent burst.

The velocity dependence of the transition to turbulence is shown in Fig. 12. Each data point represents an injection event and its color signifies the outcome: (□) for a small number of vortex lines and (■) for the

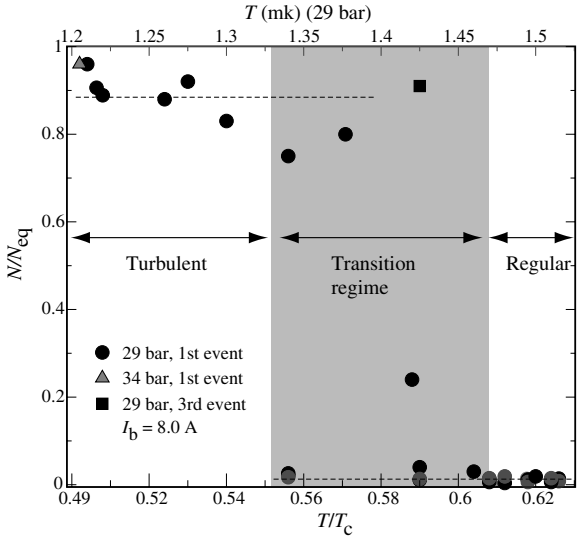

Figure 11: The final number of vortex lines measured after an injection event as a function of temperature in the transition regime. The vertical scale gives the relative vortex number $N/N_{\rm eq}$. As a function of temperature a sharp transition is observed in the final number of vortex lines.

equilibrium number of vortex lines. In the velocity range studied here the transition occurs at 0.6 $T_{\rm c}$ independent of the injection velocity in accordance with the analysis that mutual friction controls the transition.

Similar results were obtained in measurements at the other pressures, 34 and 10 bar. In Fig. 13 the results of 10, 29, 34 bar are summarized in a histogram where we have assumed that the transition is velocity independent. The half width of the transition is relatively narrow $\sim 0.03\ T_{\rm c}$. There exist mutual friction data only at two pressures: 10 and 29 bar [25, 26]. Our measurements indicate that the transition occurs roughly at $q \approx 1$. At 10 bar the transition occurs at $q = 1.3$ and at 29 bar at $q = 0.6$. In the measurements at zero pressure the slow vortex multiplication process described in Sec. 4.7 intervenes before suffciently high counterflow velocities could be generated for the KH injection process to work.

There are several factors that might influence the value of q at the transition. There is some uncertainty in the mutual friction parameters: The high magnetic field (which is required for KH injection) at the vortex loop injection site could affect the mutual friction value. Unfortunately there is no data available on the magnetic field dependence of mutual friction. The vortex core transition might influence the transition since there is a small difference in mutual friction between the two cores. There is no data on how a high magnetic field influences the vortex core transition. The neu-

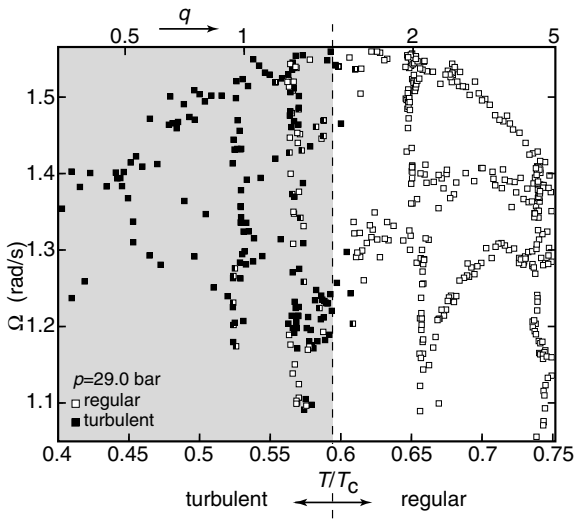

Figure 12: Transition to turbulence at 29 bar. The filled symbols (■) mark the cases where the injection resulted in almost the equilibrium number of vortex lines while the open symbols (□) represents final states with only a few vortex lines. In the velocity range studied here the transition occurs at 0.6 T_c independent of velocity. The location of the data points in the $T\Omega$-plane is determined by the KH instability and is immaterial in this context.

tron measurements which are discussed in the next section indicate that the initial vortex configuration at injection is important in starting the turbulent burst. The initial vortex configuration, for example the vortex density in the initial bundle which the shear-flow injection produces might also have differences at the two pressures.

4.4 Vortex injection with neutrons

The shear-flow instability injects a small random number of vortex loops in each event. To study the influence of the injection process itself, vortex injection from neutron absorption events [4] was also used. This is a technique which also produces locally vortex loops, but of smaller size than in the KH injection and their number can be controlled with the applied flow velocity.

The ^{3}He nucleus has a large absorption cross section for thermal neutrons. A thermal neutron has a mean free path less than 0.1 mm before it is captured by a ^{3}He nucleus which results in the nuclear reaction n+^{3}He $\rightarrow$ p+^{3}H+764 keV. The energy is released as kinetic energy of the reaction products which heat a small volume of ^{3}He to normal phase. Such "bubble" of normal liquid, less than 100 μm in diameter, cools back in microseconds to the superfluid state. During the rapid non-equilibrium cooling

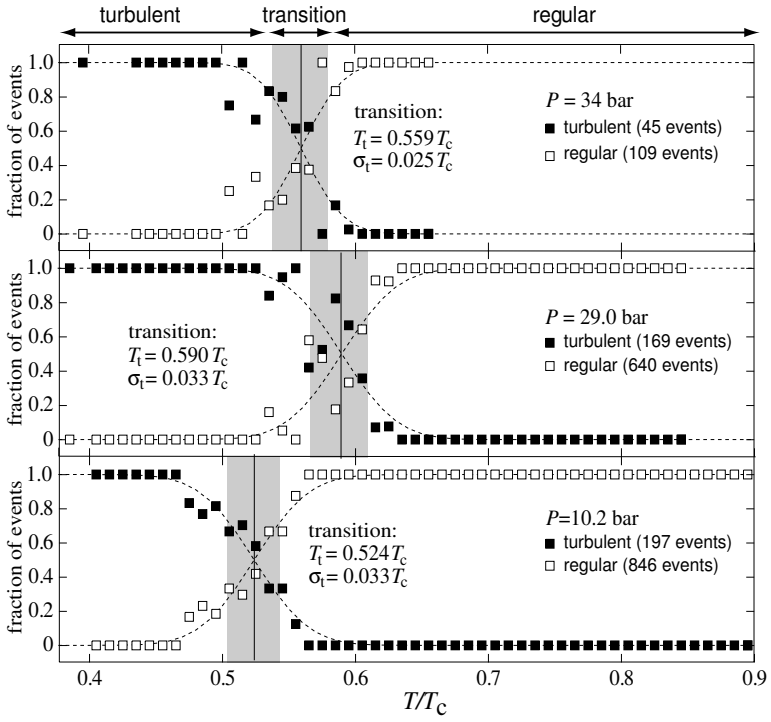

Figure 13: Transition to turbulence at different pressures. The normal distribution (with the average transition temperature T_t and dispersion σ_t) is fitted to the data in order to give an indication on the width on the transition. The transition is narrow at all pressures $\sigma_t \simeq 0.03\ T_c$. The KH injection has been used for injection.

through T_c a random vortex tangle is formed in the bubble Ref. [82]. Some of the loops in the bubble may escape into the bulk if the external flow favors the expansion of the loops. In the rotating sample the neutrons are absorbed close to the outer wall and if the counterflow velocity is sufficient, one or more loops, depending on the flow velocity, expand into the bulk.

The rate of vortex line formation was measured in [P9] at 29 bar at 0.53 T_c to be $\dot{N}_v = 0.0056[(\Omega/\Omega_{c,n})^3 - 1]\ s^{-1}$ where $\Omega_{c,n} = 1.43$ rad/s is the the minimum required flow velocity for vortex formation. As the rotation velocity is increased more neutron absorption events result into vortex formation and each event is likely to produce more vortex loops (see Ref. [83]).

Neutron injection measurements were carried out at two temperatures in the turbulent regime, at 0.53 T_c and 0.45 T_c. At 0.53 T_c below 3 rad/s vortex lines were created during neutron irradiation, but no turbulence was observed. At higher velocity turbulent bursts start to occur at random verti-

cal position in the sample. The probability distribution of how long neutron irradiation resulted in a turbulent burst was measured at $\Omega = 3.3$ rad/s at $0.53\,T_c$. Based on these measurements we conclude that about 10% of vortex injections events result in turbulence at these particular conditions [P13].

At $0.45\,T_c$ a similar measurement of the probability distribution was performed at 1.6 rad/s which is expected to be only slightly above $\Omega_{c,n}$. In this case almost all neutron absorption events that lead to vortex production result to a single loop escaping the bubble. Unfortunately the injection rate at $0.45\,T_c$ could not be measured directly because of the intervening turbulence. Nevertheless, extrapolating from the measurements at $0.53\,T_c$, we conclude that almost every injection event resulted in turbulence at $0.45\,T_c$.

These neutron measurements show that not all initial vortex configurations at injection develop into a turbulent vortex tangle close to the transition from regular to turbulent dynamics. This means that the loop configuration at injection influences the exact temperature at which the transition from regular to turbulent dynamics is observed. At sufficient initial vortex densities the transition between turbulent and regular vortex dynamics is probably close to the transition indicated by the KH injection mechanism. As the vortex density drops, the probability of turbulence decreases at a given temperature. However, by cooling to lower temperature the probability increases. At the lowest temperatures even single loops start the multiplication process. This point is discussed also in Sec. 4.7. On the other hand, turbulence cannot exist at much higher temperatures than $0.6\,T_c$ at any vortex density since at high T the injection of thousand vortex lines into high flow does not lead to the equilibrium vortex state (see Sec. 4.6).

4.5 Propagation of vortices in rotating flow

Above we investigated the conditions required for the onset of turbulence. Next we ask what happens after the localized burst of turbulence. The NMR measurements provide us some insight into what happens after the injection process. Figure 14 shows an example from NMR response as function of time after vortex lines have been injected into vortex free counterflow at $\Omega = 1.5$ rad/s. Some features can be extracted which describe the propagation and the later relaxation to the equilibrium vortex state. The first feature is the flight time, the time it takes for the vortices to travel from the injection site to the detector. The arrival of the vortex lines at the detector is indicated by the reducing absorption in the counterflow signal. The counterflow peak height drops abruptly indicating a rapid removal of the azimuthal counterflow. Simultaneously the absorption in the Larmor region shoots up and finally decays exponentially towards the equilibrium state.

According to Eq. (5) the end of a vortex line will propagate along the wall with the velocity

$$v_{L,z} = \alpha \Omega R \tag{18}$$

in rotating counterflow at the velocity $v_{\rm cf} = \Omega R$. The experiment provides the possibility to extract the time-of-flight from the injection site to the detector and thus determine the velocity at which the vortex lines travel. This allows us to extract the mutual friction parameter α from our measurements. Figure 15 displays the α values from our measurements as a function of temperature, assuming that the speed is defined by Eq. (18). These are compared to data measured in Refs. [25, 26]. Equation (18) holds when the number of vortex lines expanding in the flow is small (which is the case in high temperatures) so that the self induced velocities of the vortex lines do not contribute too much to the flow. However, there is no distinct jump in the flight time at the transition to turbulence. The equilibrium number of vortices appears to travel at close to the same velocity as a single vortex line would. The velocity of the front decreases as a function of temperature since α drops exponentially [27] with temperature.

When the vortex lines arrive to the detector, the absorption in the counterflow peak starts to reduce rapidly indicating that the global azimuthal counterflow disappears. While the counterflow disappears, the signal in the Larmor region of the NMR spectrum starts to increase with time, goes through a maximum $h_{\rm max}$ and decays exponentially towards the equilibrium signal.

The large absorption ($h_{\rm max}$) in the Larmor region during the transient process can be explained by the appearance of a z-directional superflow which is induced by the vortex lines: In addition to the axial velocity component $v_{\rm L,z} = \alpha\Omega R$, the ends of the vortex lines at the outer wall move in the azimuthal direction with the velocity $v_{{\rm L},\phi} = (1 - \alpha')\Omega R$. The spirally moving front leaves behind a helical vortex structure with a wave length which is expected to be proportional to q since $\frac{v_{{\rm L},\varphi}}{v_{\rm L,z}} = q$. Such structure induces superflow in the z-direction $v_{\rm sz}$ which in turn orients the $\hat{\mathbf{n}}$ texture such that large absorption ($h_{\rm max}$ in Fig. 14), exceeding that of a cluster of rectilinear vortex lines, is seen in the Larmor region of the NMR spectrum.

The unwinding of the twist, observed as the exponential decay, is likely to be assisted by $v_{\rm sz}$ which increases with decreasing temperature. This is a possible explanation to the counterintuitive result that the deviations from the equilibrium state relax faster at lower dissipation at lower temperature. The time constant τ of the exponential decay decreases as a function of temperature as $\propto q$. The existence of the twist is supported by the fact that the relative height of the overshoot increases $\propto q^{-1}$ with decreasing temperature [P13].

Combining all the conclusions from Fig. 14 we infer that the propagating vortices need to form a well-defined front towards the vortex-free region into which they expand. This is confirmed also by numerical simulations on the coarse-grained equation Eq. (17) [84]. According to our measurements the structure of the propagating front does not appear to display any strong

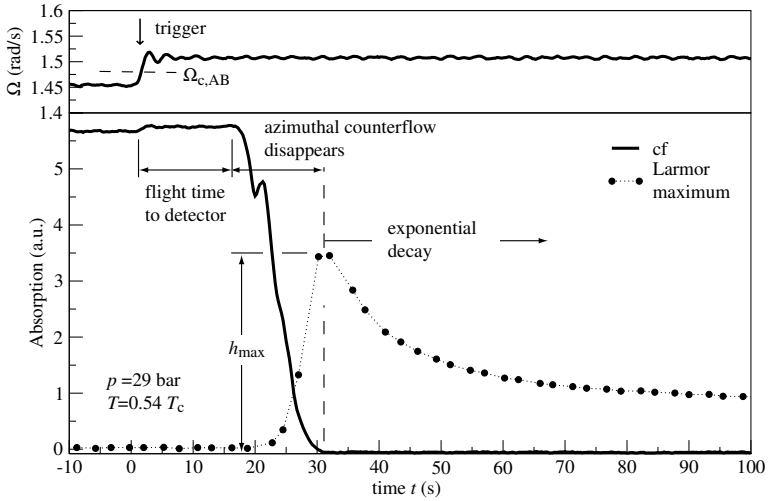

Figure 14: Measured NMR signals as a function of time when KH injection is used. A vortex free state is created (at 1.45 rad/s) just below the velocity of the shear-flow instability. Then the velocity is rapidly ramped above the critical value of the shear-flow instability (to 1.50 rad/s) (trigger), resulting in the injection of vortex loops. Since the injection occurs $\simeq$ 3 cm away from the upper end of the detector coil, the first reaction is recorded after a temperature dependent flight time. The mutual friction parameter α can be extracted from this flight time (Fig. 15). The rapid removal of the absorption in the counterflow peak (cf) indicates the removal of azimuthal counterflow. In the Larmor region the absorption overshoots simultaneously above the equilibrium value. The overshoot originates from a helical vortex state that creates a superfluid velocity component in the z-direction. Finally, the signal peak height decays exponentially towards the equilibrium value when the helix unwinds.

dependence on Ω. In this case the mutual friction is constant and the speed of propagation varies as Ω. All time dependencies associated with the front seem to have a Ω^{-1} dependence and thus the thickness of the layer is approximately constant. As a function of temperature the front appears to become thinner: The counterflow is removed in a shorter distance behind the leading edge of the front.

In neutron injection measurements there is no need for an A phase layer. Here both spectrometers monitor the same volume of B phase. The measurements show that if turbulence is started in one end of the tube, the equilibrium number of vortex lines is generated immediately, if the absorption event develops into turbulence. The vorticity moves to the vortex free flow as a front and decays to the rectilinear vortex cluster even before the front has reached the other end of the sample tube.

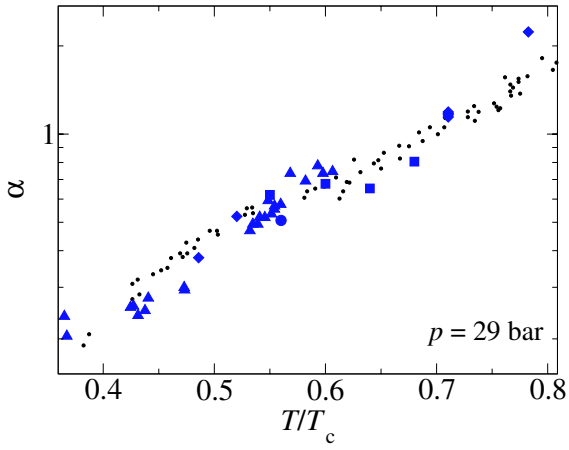

Figure 15: Mutual friction parameter α determined from flight time measurements and compared to the data from Ref. [25] (·). Here we assume that vortex lines propagate with the velocity $v_{\mathrm{L,z}} = \alpha\Omega R$. The is data measured with different methods: (▲) the time difference from the trigger of the KH instability and detection of vortex lines is measured (Fig. 14); (■) $\dot{\Omega}$ is varied (see [P8] for details); (●) measurement of the time difference between detections in the two spectrometers in neutron injection. The data marked (⧫) is measured at 34 bar. We conclude that our data is in good agreement with the data in [25] in the whole temperature range.

4.6 Massive injection events

At high temperatures injection of a few vortex loops results in the generation of equal number of vortex lines. The turbulent burst only happens in the low temperature regime. It is possible, however, to inject large numbers of vortex lines into the flow in one sudden event both at low and high temperatures. This allows a comparison between the vortex front motion at low and high temperatures.

The experimental procedure is the following: First the sample is accelerated to the target rotation velocity keeping the field in the barrier field below H_{AB} so that there is no A phase in the system. In this case the velocity necessary for vortex nucleation is high. The barrier field is slowly swept up and at some critical field value the A phase is formed in the sample. When the A phase is formed the critical velocity of the KH instability is at its lowest (Fig. 9), the AB boundary is unstable, and a sudden massive instability follows. A large burst of vortex lines is injected at once in the B phase so that the boundary stabilizes. Depending on the rotation speed the number of injected vortex lines can be a thousand or more. The number is, however, not yet the equilibrium number since vortex creation appears to stop when

the injection stops. Even injecting thousands of vortex lines at $T > 0.6\ T_{\rm c}$, the final state is not the equilibrium vortex state which is the most common result after vortex injection in the turbulent temperature regime.

4.7 Multiplication of isolated vortex lines in applied flow

At higher temperatures in the turbulent regime ($0.5 \lesssim T/T_c \lesssim 0.6$) high counterflow velocities can be formed rather conveniently. Small remnant loops, if there are any, do not necessarily lead to a turbulent burst as indicated by the neutron injection experiments. On cooling down further the situation starts to change. In many cases the experimental volume seems to fill with vortex lines already at low rotation.

Figure 16 shows an experiment where the equilibrium cluster of vortex lines at $\Omega_{\rm i} = 0.05$ rad/s is accelerated rapidly to a higher velocity $\Omega_{\rm f}$. A slow increase in the number of vortex lines is observed to follow. This first initial process is very different in character from the turbulent bursts which were discussed earlier where the equilibrium number of vortex lines are generated in the matter of seconds. In Fig. 16 the slow increase continues for over 200 s in the case when $\Omega_{\rm f} = 0.6$ rad/s. It is finally terminated in an abrupt change in the rate of vortex formation which we interpret as a turbulent burst that finally generates the equilibrium number of vortex lines. This slow multiplication process is similarly observed if the sample is accelerated from zero velocity, provided that there are suitable seed loops present in the sample.

The process is associated with such sections of vortex lines that are not rectilinear and are not part of the vortex cluster but connect to the cylindrical side wall. This was verified by cooling a small cluster of vortex lines under rotation to the temperature region where the slow process is prominent. The cluster was prepared at high temperatures and confined by counterflow such that there were only rectilinear lines present. No increase of vortex number was observed until the velocity decreased such that the cluster expanded to the annihilation threshold - some vortex lines came into contact with the cylindrical container wall - and the velocity was increased back.

We interpret the slow multiplication to be mainly associated with isolated vortex lines reconnecting with the wall. The process is started by a vortex which expands in the applied flow to become a rectilinear line. Kelvin waves are exited and eventually reconnect with the walls and create a new vortex loop. Reconnections are known to excite Kelvin waves [29] and thus the process continues. Although a single loop is observed to be stable in homogenous flow (see for example [85]) in suitable flow a single loop can become unstable towards reconnections [86]. Once sufficient vortex density is generated in the annular counterflow volume outside the cluster of rectilinear vortex lines (see Fig. 3)) vortex-vortex interactions become significant

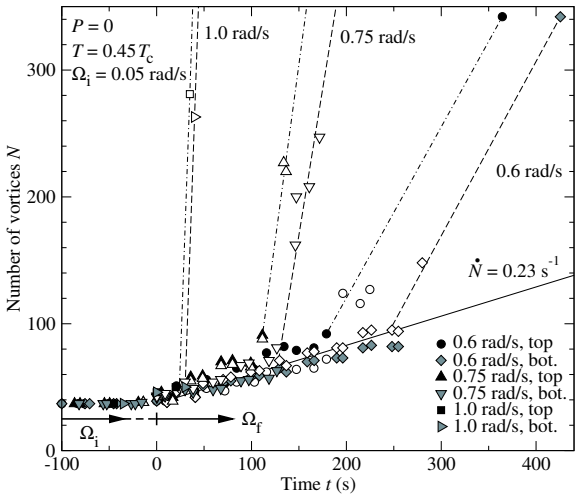

Figure 16: Examples of a slow increase in the vortex number. The vortex number is measured simultaneously with both spectrometers. Solid symbols refer to the experimental calibration of the vortex number while open symbols refer to a theoretical calibration. The rotation velocity is increased from an initial $\Omega_{\rm i}$=0.05 rad/s to three different final velocities $\Omega_{\rm f}$. A slow increase in the vortex number follows which lasts for more than 200 s in the case of $\Omega_{\rm f}$ = 0.6 rad/s. The slow process acts as a precursor to turbulence which is seen as a rapid increase in the vortex number, indicated by the dashed lines which are a guide to the eye. The initial state is the equilibrium state at $\Omega_{\rm i}$=0.05 rad/s. It is prepared by letting a large number of vortex lines annihilate to the equilibrium cluster of $N \approx 37$ vortex lines at $\Omega_{\rm i}$=0.05 rad/s. In the equilibrium vortex state there are some vortex lines that curve to the cylindrical outer boundary because nonidealities in the sample setup (The sample is slightly tilted, for example.). The vortex lines that are curved to the wall start to expand in the increased counterflow towards rectilinear lines and during this process increase the vortex number through reconnections [P12]. A similar slow increase in the vortex number can also be observed when $\Omega_{\rm i} = 0$ provided that there are suitable seed loops present in the sample.

and a turbulent burst follows.

There are two related reasons why the linear vortex multiplication process occurs at low temperatures both connected to the exponentially vanishing mutual friction damping. First, vortex lines become easily destabilized by Kelvin wave excitations which are generated by reconnection kinks; while at high damping corrugations smooth out rapidly and are not able to propagate. The second contributing effect is that as dissipation decreases, it can take hours for the last vortex line to annihilate at the sample boundary in the absence of applied flow. This is not caused by surface pinning, mutual friction has just dropped to such low value that the last vortex line evolves exceedingly slowly in the absence of any flow. This fact creates a new challenge for rotating experiments at low temperatures in ^{3}He-B: To prepare vortex-free flow states becomes increasingly difficult as the temperature decreases.

5 Conclusions

This thesis examines two aspects of hydrodynamics in superfluid ^{3}He. First, the interface of the A and the B phases was studied when a shear-flow across the boundary in the superfluid components was imposed. This led to the first demonstration of the analog of the classical Kelvin-Helmholtz instability in superfluids. The instability turned out to provide unprecedented flexibility in vortex injection into ^{3}He-B under vortex free counterflow. As result, the transition between regular and turbulent vortex dynamics was discovered, which is the main focus of this thesis.

The experiment on the AB phase boundary showed that the vortex structures in the A phase do not easily penetrate to the B phase side. Instead, there is a well-defined critical velocity when this happens. The penetration mechanism turned out to be the analog of the Kelvin-Helmholtz instability known from regular hydrodynamics. It is the first example of the instability when no viscosity is present in the initial state.

The work on turbulence in ^{3}He-B showed a transition from vortex dynamics that might be described as laminar to what usually is considered as turbulent. The experiments and the analysis indicate that at sufficiently high velocity the transition to turbulent flow is controlled by the temperature dependent mutual friction, a property intrinsic to the liquid. The relevant combination of parameters is identified as $q = \alpha/(1 - \alpha')$. Although, in retrospect, the transition was expected and had been observed often before, the criteria for turbulence became evident in only these experiments.

Experiments with various vortex injection methods indicate that the initial vortex configuration is also important for the initiation of turbulence. At higher temperatures, in the turbulent regime, the initialization of turbulence requires some number of vortex lines. If the vortex density is not sufficient the lines disperse and merely move to the minimum energy configuration without notable reconnections. The turbulence is triggered more and more easily with reducing temperature and eventually, according to our measurements, even a single vortex which expands in applied rotating flow becomes unstable towards reconnections.

In these experiments we also investigated the question how large numbers of vortex lines expand into a rotating sample of vortex free superfluid. In other words how the superfluid component spins up to co-rotation with the normal component. The vortex lines appear to move into the vortex free counterflow as a front. The spiralling motion of the vortex lines in the front leaves behind a helical vortex structure that eventually decays to the equilibrium vortex cluster.

There are still open questions regarding both the Kelvin-Helmholtz instability and turbulent vortex dynamics. For example, what happens to the KH instability in the $T \to 0$ limit, how will it develop then? What will happen to the instability in the shallow water limit? There has even been

a suggestion that the instability could be used for an analog model of a black hole [3]. Concerning turbulent vortex dynamics, additional measurements are needed on how the helical vortex cluster unwinds as a function of time or propagation distance. Is there an unwinding region that follows the front or is the decay dominated by the solid top and bottom plates of the sample container? This could be answered by relatively simple geometric modifications of the setup and more measurements using neutron injection. The rate of slow vortex production and its temperature dependence have not been studied carefully. All measurements described here are limited to above 0.4 T_c. Measurements closer to the $T \rightarrow 0$ limit would be important to clarify what changes occur in the vortex dynamics when the normal component vanishes.

Considering measurement techniques, this work clarifies some of the challenges when ^{3}He-B is studied under rotation at low temperatures. First, the vortex dynamics changes such that it becomes exceedingly more difficult to create the rotating counterflow state. Injection of even a single vortex loop may lead to sudden formation of the equilibrium cluster of vortex lines through reconnections. In the low temperature limit, the NMR measurement of vortices in the ^{3}He-B sample starts to fail also. The changes in the spectrum created by vortices or counterflow disappear already above 0.30 T_c rendering the current NMR technique as such not useful.

References

[1] P. L. Kapitza, Nature **141**, 74 (1938).

[2] D. D. Osheroff, R. C. Richardson, and D. M. Lee, Phys. Rev. Lett. **28**, 885 (1972).

[3] G. E. Volovik, *The Universe in a Helium Droplet* (Oxford University Press, Oxford, UK, 2003).

[4] V. M. H. Ruutu, V. B. Eltsov, A. J. Gill, T. W. B. Kibble, M. Krusius, Y. M. Makhlin, B. Placais, G. E. Volovik, and W. Xu, Nature **382**, 334 (1996).

[5] E. M. Lifshitz and L. P. Pitaevskii, *Statistical Physics part 2, Landau and Lifshitz course of Theoretical physics* (Pergamon Press, Oxfrd, UK, 1980).

[6] J. Bardeen, L. N. Cooper, and J. R. Schrieffer, Phys. Rev. **108**, 1175 (1957).

[7] I. Hahn, Ph.D. thesis, University of Southern California, 1993, unpublished.

[8] J. P. Pekola, J. T. Simola, P. J. Hakonen, M. Krusius, O. V. Lounasmaa, K. K. Nummila, G. Mamniashvili, R. E. Packard, and G. E. Volovik, Phys. Rev. Lett. **53**, 584 (1984).

[9] P. W. Anderson and W. F. Brinkman, Phys. Rev. Lett. **30**, 1108 (1973).

[10] E. V. Thuneberg, Physica B **178**, 168 (1992).

[11] R. Balian and N. R. Werthamer, Phys. Rev. **131**, 1553 (1963).

[12] D. V. Osbourne, Proc. Phys. Soc. **A63**, 909 (1950).

[13] L. Onsager, Nuovo Cimento **6**, 249 (1949).

[14] R. Feynman, in *Progress in Low Temperature Physics*, edited by C. Gorter (North Holland, Amsterdam, 1955), Vol. 1, p. 36.

[15] C. F. Barenghi, R. J. Donnelly, and W. F. Vinen, J. Low Temp. Phys. **124**, 123 (2001).

[16] E. V. Thuneberg, Phys. Rev. Lett. **56**, 359 (1986).

[17] Y. Kondo, J. S. Korhonen, M. Krusius, V. V. Dmitriev, E. V. Thuneberg, and G. E. Volovik, Phys. Rev. Lett. **68**, 3331 (1992).

[18] N. D. Mermin and T. L. Ho, Phys. Rev. Lett. **36**, 594 (1976).

[19] P. J. Hakonen, O. T. Ikkala, S. T. Islander, O. V. Lounasmaa, T. K. Markkula, P. Roubeau, K. M. Saloheimo, and G. E. Volovik, Phys. Rev. Lett. **48**, 1838 (1981).

[20] Ü. Parts, , J. M. Karimäki, J. H. Koivuniemi, M. Krusius, V. M. H. Ruutu, E. V. Thuneberg, and G. E. Volovik, Phys. Rev. Lett. **75**, 3320 (1995).

[21] R. Blaauwgeers, V. B. Eltsov, M. Krusius, J. J. Ruohio, R. Schanen, and G. E. Volovik, Nature **404**, 471 (2000).

[22] Ü. Parts, E. V. Thuneberg, G. E. Volovik, V. M. H. Ruutu, M. Heinilä, J. M. Karimäki, and M. Krusius, Phys. Rev. Lett. **72**, 3839 (1994).

[23] D. R. Tilley and J. Tilley, *Superfluidity and superconductivity*, 3rd ed. (IOP Publishing, Bristol, UK, 1990).

[24] R. J. Donnelly, *Quantized vortices in helium II* (Cambridge University Press, Cambridge, UK, 1991).

[25] T. D. C. Bevan, A. J. Manninen, J. B. Cook, H. Alles, J. R. Hook, and H. E. Hall, J. Low Temp. Phys. **109**, 423 (1997).

[26] T. D. C. Bevan, A. J. Manninen, J. B. Cook, A. J. Armstrong, J. R. Hook, and H. E. Hall, Phys. Rev. Lett. **74**, 750 (1995), (correction **74**, 3092, 1995).

[27] N. B. Kopnin, Rep. Prog. Phys. **65**, 1633 (2002).

[28] R. J. Donnelly and C. F. Barenghi, J. Phys. Chem. Ref. Data **27**, 1217 (1998).

[29] B. V. Svistunov, Phys. Rev. B **52**, 3647 (1995).

[30] W. I. Glaberson, W. W. Johnson, and R. M. Ostermeyer, Phys. Rev. Lett. **33**, 1197 (1974).

[31] R. M. Ostermeyer and W. I. Glaberson, J. Low Temp. Phys. **21**, 191 (1975).

[32] E. R. Dobbs, *Helium Three* (Oxford University Press, Oxford, UK, 2000).

[33] V. M. H. Ruutu, Ü. Parts, J. Koivuniemi, N. B. Kopnin, and M. Krusius, J. Low Temp. Phys. **107**, 93 (1997).

[34] D. D. Awschalom and K. W. Schwarz, Phys. Rev. Lett. **52**, 49 (1984).

[35] E. Varoquaux, O. Avanel, Y. Mukharski, and P. Hakonen, in *Quantized Vortex Dynamics and Superfluid Turbulence*, edited by C. F. Barenghi, R. J. Donnelly, and W. F. Vinen (Springer, Berlin, 2000).

[36] A. J. Leggett, Ann. Phys. **85**, 11 (1974).

[37] V. M. H. Ruutu, Ü. Parts, and M. Krusius, J. Low Temp. Phys. **103**, 331 (1996).

[38] V. B. Eltsov, R. Blaauwgeers, M. Krusius, J. J. Ruohio, and R. Schanen, J. Low Temp. Phys. **124**, 123 (2001).

[39] J. Kopu, R. Schanen, R. Blaauwgeers, V. B. Eltsov, M. Krusius, J. J. Ruohio, and E. V. Thuneberg, J. Low Temp. Phys. **120**, 213 (2000).

[40] H. Smith, W. F. Brinkman, and S. Engelberg, Phys. Rev. B **15**, 199 (1977).

[41] D. D. Osheroff, Physica B **90**, 20 (1977).

[42] J. S. Korhonen, A. D. Gongadze, Z. Janu, Y. Kondo, M. Krusius, and Y. M. Mukharski, Phys. Rev. Lett. **65**, 1211 (1990).

[43] Ü. Parts, V. M. H. Ruutu, J. H. Koivuniemi, Y. M. Bunkov, V. V. Dimitriev, M. Fogelstrom, M. Huebner, Y. Kondo, N. B. Kopnin, J. S. Korhonen, M. Krusius, O. V. Lounasmaa, P. I. Soininen, and G. E. Volovik, Europhys. Lett. **31**, 449 (1995).

[44] P. J. Hakonen, M. Krusius, M. M. Salomaa, R. H. Salmelin, J. T. Simola, A. D. Gongadze, G. E. Vachnadze, and G. A. Kharadze, J. Low Temp. Phys. **76**, 225 (1989).

[45] P. J. Hakonen, O. T. Ikkala, S. T. Islander, T. K. Markkula, P. M. Roubeau, K. M. Saloheimo, D. I. Garibashvili, and J. S. Tsakadze, Cryogenics **23**, 234 (1983).

[46] F. Pobell, *Matter and Methods at Low Temperatures* (Springer-Verlag, Berlin, Germany, 1992).

[47] *High-Q surface mount capacitors*, Spectrum Control Inc., 6000 West Ridge Road, Erie, PA 16506.

[48] A. Abragam, *Principles of nuclear magnetism* (Oxford university press, Oxford, UK, 1961).

[49] J. Koivuniemi, Ph.D. thesis, Helsinki Univesity of Technology, 1998.

[50] V. Ruutu, J. Koivuniemi, Ü. Parts, A. Hirai, and M. Krusius, Physica B **194-196**, 159 (1994).

[51] J. Koivuniemi, M. Kiviranta, H. Seppä, and M. Krusius, J. Low Temp. Phys. **110**, 255 (1998).

[52] S. M. Sze, *VLSI Technology* (McGraw-Hill, New York, USA, 1983).

[53] J. Knobloch, in *Hydrogen in materials and Vacuum Systems*, edited by G. R. Myneni (Springer Verlag, Berlin, 2003), Chap. The Q disease in Superconducting Niobium RF Cavities, pp. 133–149.

[54] Ü. Parts, Y. Kondo, J. S. Korhonen, M. Krusius, and E. V. Thuneberg, Phys. Rev. Lett. **71**, 2951 (1993).

[55] P. Schiffer, M. T. O'Keefe, M. D. Hildreth, H. Fukuyama, and D. D. Osheroff, Phys. Rev. Lett. **69**, 120 (1992).

[56] Lord Kelvin (Sir William Thomson), *Hydrodynamics and General Dynamics* (Cambridge University Press, Cambridge, UK, 1910), Vol. 4.

[57] G. E. Volovik, JETP Letters **75**, 491 (2002).

[58] J. Zhang, S. Childress, A. Libchaber, and M. Shelley, Nature **408**, 835 (2000).

[59] D. D. Osheroff and M. C. Gross, Phys. Rev. Lett. **38**, 905 (1977).

[60] D. Vollhardt and P. Wölfle, *The Superfluid Phases of Helium 3* (Taylor and Francis, London, 1990).

[61] I. Hahn, S. T. P. Boyd, H. Bozler, and C. M. Gould, Phys. Rev. Lett. **81**, 618 (1998).

[62] L. D. Landay and E. M. Lifshitz, *Fluid Mechanics*, 2nd ed. (Pergamon Press, Oxford, UK, 1987).

[63] T. E. Faber, *Fluid dynamics for physicists* (Cambridge University Press, Cambridge, 1995).

[64] B. Hof, A. Juel, and T. Mullin, Phys. Rev. Lett. **91**, 244502 (2003).

[65] K. W. Schwarz, Phys. Rev. B **38**, 2398 (1988).

[66] C. J. Gorter and J. H. Mellink, Physica **15**, 285 (1949).

[67] W. F. Vinen, Proc. R. Soc. London Ser. A. **242**, 493 (1957).

[68] S. R. Stalp, L. Skrbek, and R. J. Donnelly, Phys. Rev. Lett. **82**, 4831 (1999).

[69] L. Skrbek, J. J. Niemela, and R. J. Donnelly, Phys. Rev. Lett. **85**, 2973 (2000).

[70] W. F. Vinen, Phys. Rev. B **61**, 1410 (2000).

[71] W. F. Vinen and J. Niemela, J. Low Temp. Phys. **128**, 167 (2002).

[72] M. Niemetz and W. Schoepe, J. Low Temp. Phys. **135**, 447 (2004).

[73] W. F. Vinen, Phys. Rev. B **71**, 24513 (2005).

[74] V. S. L'vov, S. V. Nazarenko, and G. E. Volovik, JETP Letters **80**, 546 (2004).

[75] S. N. Fisher, A. Hale, A. M. Guénault, and G. R. Pickett, Phys. Rev. Lett. **86**, 244 (2001).

[76] D. I. Bradley, S. N. Fisher, A. M. Guénault, M. Lowe, G. R. Pickett, and A. Rahm, J. Low Temp. Phys. **124**, 113 (2001).

[77] D. I. Bradley, S. N. Fisher, A. M. Guénault, M. R. Lowe, G. R. Pickett, A. Rahm, and R. C. V. Whitehead, Phys. Rev. Lett. **93**, 235302 (2004).

[78] E. R. Benton and A. C. Jr, Annu. Rev. Fluid Mech. **6**, 257 (1974).

[79] H. P. Greenspan, *The theory of rotating fluids* (Cambridge University Press, Cambridge, UK, 1968).

[80] E. B. Sonin, Rev. Mod. Phys. **59**, 87 (1987).

[81] N. B. Kopnin, Phys. Rev. Lett. **92**, 135301 (2004).

[82] W. H. Zurek, Nature **317**, 505 (1985).

[83] V. M. Ruutu, V. B. Eltsov, M. Krusius, Y. G. M. B. Plaçais, and G. E. Volovik, Phys. Rev. Lett. **80**, 1465 (1998).

[84] V. B. Eltsov, to be published .

[85] D. Kivotides, C. F. Barenghi, and D. C. Samuels, Phys. Rev. Lett. **290**, 777 (2000).

[86] D. C. Samuels, Phys. Rev. B **47**, 1107 (1993).